Title
On the scaling of air entrainment from a ventilated partial cavity

Journal
Journal of Fluid Mechanics, 732

ISSN
0022-1120

Authors
Mäkiharju, Simo A
Elbing, Brian R
Wiggins, Andrew
et al.

Publication Date
2013-10-10

DOI
10.1017/jfm.2013.387

On the Scaling of Air Entrainment from a Ventilated Partial Cavity

Journal:	*Journal of Fluid Mechanics*
Manuscript ID:	JFM-12-S-1238.R2
mss type:	Standard
Date Submitted by the Author:	n/a
Complete List of Authors:	Mäkiharju, Simo; University of Michigan, Mechanical Engineering Elbing, Brian; Oklahoma State University, Mechanical Engineering, Wiggins, Andrew; University of Michigan, Naval Architecture and Marine Engineering Schinasi, Sarah; University of Michigan, Naval Architecture and Marine Engineering Vanden-Broeck, Jean-Marc; University College London, Mathematics Perlin, Marc; University of Michigan, Naval Architecture and Marine Engineering; Mechanical Engineering Dowling, David; University of Michigan, Mechanical Engineering; Naval Architecture and Marine Engineering Ceccio, Steven; University of Michigan, Naval Architecture and Marine Engineering; Mechanical Engineering
Keyword:	Drag reduction < Flow Control, Gas/liquid flows < Multiphase and Particle-laden Flows

On the Scaling of Air Entrainment from a Ventilated Partial Cavity

Simo A. Mäkiharju[1], Brian R. Elbing[3], Andrew Wiggins[2], Sarah Schinasi[2],
Jean-Marc Vanden-Broeck[4], Marc Perlin[2,1], David R. Dowling[1,2] and Steven L. Ceccio[1,2]

[1]Mechanical Engineering, University of Michigan, Ann Arbor, MI 48109, USA
[2]Naval Architecture and Marine Engineering, University of Michigan, Ann Arbor, MI 48109, USA
[3] Mechanical Engineering, Oklahoma State University, Stillwater, OK 74078, USA
[4]Mathematics Department, University College London, London WC1E 6BT, UK

Corresponding author: Simo Mäkiharju, smakihar@umich.edu

Submitted to the *Journal of Fluid Mechanics*

Abstract

The behavior of a nominally two-dimensional ventilated partial cavity was examined over a wide range of size scales and flow speeds to determine the influence of Froude, Reynolds, and Weber number on the cavity shape, dynamics, and gas entrainment rate. Two geometrically similar experiments were conducted with a 14:1 length-scale ratio. The results were compared to a two-dimensional semi-analytical model of the cavity flow, and Froude scaling was found to be sufficient to match basic cavity shapes. However, the air flux required to maintain a stable cavity did not scale with Froude number alone, as the dynamics of the cavity closure changed with increasing Reynolds number. The required air flux differed over one order of magnitude between the lowest and highest Reynolds number flows. But, for sufficiently high Reynolds numbers, the rate of scaled entrainment between appeared to approach Reynolds number independence. Modest changes in surface tension of the small-scale experiment suggested that the Weber number was important only at the lowest speeds and smaller length scale. Otherwise, the Weber numbers of the flows were sufficiently high to make the effects of interfacial tension negligible. We also observed that modest unsteadiness in the inflow to the large-scale cavity led to a

significant increase in the required air flux needed to maintain a stable cavity, with the required excess gas flux nominally proportional to the flow's perturbation amplitude. Finally, discussion is provided on how these results relate to model testing of Partial Cavity Drag Reduction (PCDR) systems for surface ships.

1. Introduction

Shipping is vital for global commerce, as it is generally one of the most economical and environmentally friendly transportation methods for raw materials, oil, natural gas and durable goods. As approximately 60% of a typical surface ship's propulsive power is required to overcome friction drag, it is desirable to reduce the friction drag by either passive or active means. Passive methods of friction drag reduction include the reduction of surface roughness on the ship hull, and the application of structured and compliant surfaces (Choi, 1996). Active methods for friction drag reduction include the injection of special substances into the boundary flow around the hull with the usual intent being modification of the turbulent transport of momentum across the hull boundary layer. In particular, the effects of injecting high-molecular weight polymeric solutions has been studied extensively (for example see: White and Mungal 2008; Winkel *et al.* 2009; White *et al.* 2012).

Injection or formation of gas near the hull of marine vehicles has also been shown to significantly reduce skin friction. These methods are generally referred to as "air lubrication" and have been reviewed recently by Ceccio (2010). Air lubrication can be divided into three main subcategories: Bubble Drag Reduction (BDR) (Madavan *et al.*, 1985; Kodama *et al.*, 2000; Sanders *et al.*, 2006); Air Layer Drag Reduction (ALDR) (Elbing *et al.*, 2008); and Partial

Cavity Drag Reduction (PCDR) (Butuzov, 1967; Matveev, 2007; Gokcay *et al.* 2004; Lay *et al.*, 2010; Gorbachev and Amromin, 2012). Successful applications of air lubrication usually involve the separation of the liquid flow from the hull by a macroscopic layer of air, vapor, and/or other gas. Alternatively, a free surface may form adjacent to the hull or over the bulk of a submerged body. For high-speed craft, such free surfaces can be achieved through cavitation, which forms a natural partial cavity or a super cavity. However, for surface ships moving at speeds on the order of 40 knots or less, such natural cavities will not readily occur (Amromin and Mizine, 2003). For slower surface craft, recesses in the hull can capture a large volume of non-condensable gas (such as for Surface-Effect Ships), and this reduces the wetted surface of the ship and results in reduced friction drag.

Interestingly, cavity flows similar to PCDR occur under the flow of dam spillways (Chanson, 1996). However, for PCDR applications, gravity always acts to stabilize the interface, pressure in the cavity is nearly at equilibrium with that of the flow and gas is supplied at sufficiently high fluxes that the shear between the two phases is lessened. Hence, the observed qualitative behavior (*e.g.* significance of entrainment through the interface *versus* from the closure) and required gas fluxes can be significantly different.

Implementation of PCDR on a surface ship hull requires the formation of one or more gas cavities beneath the hull. A series of rigid chambers (or “niches”) placed on the bottom of the hull can be supplied with gas. A properly designed chamber would allow the liquid flow to separate cleanly from the hull to form a free surface, and then reattach smoothly to the hull downstream at the cavity closure. The cavity interface is a free surface that often exhibits waves in the streamwise and transverse directions. The streamwise profile may consist of a partial wave or multiple waves crests before it impinges on the hull at the cavity closure (Matveev, 2007).

Ideally, the liquid flow reattaches on the hull in such a way that the gas lost and the form drag that occurs due to liquid-flow impingement are both minimized at the cavity closure.

Ships employing PCDR continue to be developed (Evangelista, 2011; Foeth, 2011), but traditional model-scale testing of hull forms employing PCDR are challenging. Models of hull forms can be readily Froude scaled, but the cavity flow and resulting gas entrainment at the cavity closures is not expected to scale in a similar way. Additionally, the gas loss rate must be manageable when the ship is undergoing motion in a seaway, so it is important to understand how the partial cavity and gas entrainment rate are affected by unsteady inflows. Partial cavities in steady and perturbed flows have been studied with small-scale experiments (Kopriva *et al.*, 2008; Arndt *et al.*, 2009). Larger-scale observations and comparisons with smaller scale tests are needed and are provided here.

In the present study we examine flows of single-wave partial cavities formed on geometrically similar test configurations with a length-scale ratio of 14:1, which permits us to reveal differences in the cavity dynamics and gas entrainment rates for Froude scaled cavities over a Reynolds number range from 1 to 80 million. Additionally the effects of inflow perturbations and surface tension were examined at the large and small scales, respectively. The rest of this manuscript is organized into five additional sections. The basic test model geometry, expected cavity shape, and numerical model and its results are described Section 2. The large-scale and small-scale experiments are described in Sections 3 and 4, respectively. The results and scaling of these two experiments are discussed in Section 5, and our conclusions are presented in Section 6.

2. The Basic Cavity Flow and Scaling Parameters

A schematic diagram of the experimental setup and cavity is shown in figure 1. The principal dimensions and flow parameters are presented in tables 1 and 2, respectively, for the two experimental setups. The cavity is formed beneath a flat plate equipped with a backward facing step (behind which the cavity forms) and a *beach* or *cavity arrestor* to facilitate smooth closure of the cavity. The model is similar to that described in Lay *et al.* (2010). As the cavity starts at the step and closes on the beach, air is injected at the base of the step to first establish and then maintain the cavity. Air is entrained at the trailing edge of the cavity as the liquid flow impinges on the beach. In the current experiments the beach height, H_B, is one-half of the step height, H. From the base of the step to the crest of the beach, we define a nominal stable cavity length L. The model is placed in a flow channel with nearly square cross-section; hence the cavity flow is of finite depth and span. The depth of the flow upstream of the step is D, and the span of the model is W. Finally, in the present experiments, a flow gate with an actuated flap was installed upstream of the large-scale test model to produce a free-surface over the test model to allow for the discharge of the injected air and to create perturbations of the incoming flow. Details of both the large and small-scale experimental setups are provided in Sections 3 and 4, respectively.

2.1 The Two-Dimensional Cavity Profile

The scaling of partial cavity flows is often accomplished with the Froude number based on the cavity length, L, such that $Fr_L = U/(gL)^{1/2}$, where U is the freestream speed and g is the gravitational acceleration. This is an appropriate scaling for semi-infinite cavity flows, such as the free surface that forms downstream of the transom of a ship, as discussed by Maki *et al.* (2008). However, unlike a ship at sea, the cavity detachment in the present study occurs at a finite depth given the finite size of the water channel test section and is not at atmospheric pressure, but at the static pressure at the cavity depth. Therefore, the flow both upstream and downstream of the cavity detachment can be supercritical. Thus, for all conditions examined in the present study and for weakly supercritical flows, the cavity flow might become similar to an undular hydraulic jump, as discussed by Ohtsu *et al.* (2001) and White (2001). Therefore, for these experiments, it is important to consider the Froude number based on the inlet channel depth, D (see figure 1), such that $Fr_D = U/(gD)^{1/2}$. The experiments described here were conducted mostly in the undular or weak jump regime, as Froude number based on the incoming depth ranged from $1.4 < Fr_D < 2.7$. Despite the finite depth of the channel, we expect that the gas entrainment processes at the cavity closure are similar to those of a cavity in deep water since the gas flux at the cavity closure is governed primarily by the turbulent flow within the closure region, where the free stream speed, properties of the fluids and the angle at which the cavity meets the beach are of primary significance. Hence, we postulate that the flow geometry used here can yield relevant information for PCDR flows on surface ships.

Note that the cavity length is dependent on the Froude number – based on any fixed length scale – such that at low Fr, the liquid-flow wave crest may impinge on the model upstream of the beach (producing early cavity closure), while at high Fr the cavity may extend beyond the beach. Therefore, for any given cavity geometry we expect that there will be an optimal range of Fr where the free surface of the cavity will extend to the beach and close smoothly, reducing the rate of gas entrainment at the cavity closure and, hence, the amount of injected gas necessary to maintain a stable cavity. Here, the term *cavity closure* refers to the location where the cavity essentially terminates and the liquid flow impinges on the test model. There can still exist shed pockets of gas or even a nearly continuous gas layer downstream of the closure. Also, we note that in the calculations, the cavity gas pressure is assumed matched to the static pressure of the flow at the cavity separation. As we shall see later, this assumption is supported by the experimental observations for the cavities studied.

2.2 Formulation of Numerical Model to Predict the Cavity Surface Profile

To aid with the initial design of the hull shape of a ship utilizing PCDR, it is desirable to have a relatively simple model that can be used to predict the overall cavity shape for given flow conditions, and here we discuss one such model. The liquid flow beneath the step is modeled as a free surface flow emerging from under a semi-infinite flat plate in water of finite depth. The free surface is "closed" downstream with a second semi-infinite plate (figure 2). There is then one point where the free surface separates from the upstream plate and one point where it reattaches to the downstream plate. In the experiment these points occur at the edge of backward facing step and on the beach, respectively. In the numerical model, both of the semi-infinite plates are horizontal. The Cartesian coordinates are oriented with the x-axis along the semi-infinite plate and the Y-axis directed vertically upwards. For the numerical model the origin is chosen to be at the separation point, and the X and Y – coordinates used in these calculations are related to the dimensional x and y – coordinate by $X = x/D$ and $Y = (H-y)/D$, respectively. (*I.e.* the X and Y – coordinates are non-dimensionalized by the flow depth at the backward facing step, D.) Here, both the X and Y-coordinates of the re-attachment location are part of the solution. Gravity acts vertically downwards and surface tension is neglected. The flowing water is assumed incompressible, inviscid, and irrotational. Therefore the fluid velocity can be obtained from the potential function $\phi(X,Y)$ or stream function $\psi(X,Y)$ via

$$u = \frac{\partial \phi}{\partial X} = \frac{\partial \psi}{\partial Y} \text{ , and} \tag{2.1}$$

$$v = \frac{\partial \phi}{\partial Y} = -\frac{\partial \psi}{\partial X} \ . \tag{2.2}$$

Here u and v denote the X and Y components of the velocity. Without loss of generality one can choose $\phi = 0$ at the separation point and $\psi = 0$ on the free surface and along the semi-infinite plates. As $X \to -\infty$, the flow approaches a uniform stream with constant velocity U and constant depth D. As the dimensionless variables are defined by choosing U as the reference velocity and D as the reference length, it follows that $\psi = -1$ on the test section bottom. The complex potential is defined as

$$f = \phi + i\psi \, . \tag{2.3}$$

On the free surface the pressure is constant and, in dimensionless variables, the dynamic boundary condition yields

$$\frac{1}{2}\left(u^2 + v^2\right) + \frac{1}{{Fr_D}^2} Y = B \, , \tag{2.4}$$

where B is the Bernoulli constant and Fr_D is the Froude number defined by

$$Fr_D = \frac{U}{(gD)^{1/2}} \ . \tag{2.5}$$

The problem is solved by a boundary integral equation method. A similar approach was used by Vanden-Broeck (1980), Vanden-Broeck (1996) and others (see Vanden-Broeck (2010) for a review and further references). The complex velocity is $w = u - iv$, and can be related to a quantity $\tau - i\theta$ by the relation

$$u - iv = e^{\tau - i\theta} \quad , \tag{2.6}$$

and ϕ and ψ are chosen as independent variables. It follows from (2.1) and (2.2) that the complex quantity $\tau - i\theta$ is an analytic function of f in the strip $-1 < \psi < 0$ of the complex f-plane. The strip $-1 < \psi < 0$ of the complex potential plane is then mapped into the upper half of the complex plane $\alpha + i\beta$ by the conformal mapping

$$\alpha + i\beta = e^{-\pi f} = e^{-\pi\phi} e^{-i\pi\psi} \tag{2.7}$$

The free surface is mapped onto the portion $\alpha_c < \alpha < 1$ of the α-axis. Here $\alpha_c = e^{-\pi\phi_c}$, where ϕ_c is the value of ϕ at the separation point. The bottom is mapped onto the negative α-axis and the right and left plates onto the portions $0 < \alpha < \alpha_c$ and $\alpha > 1$ of the α - axis.

The Cauchy integral formula is applied to the function $\tau - i\theta$ in the complex $\alpha + i\beta$ plane. The contour is chosen such that it consists of the real axis and a semicircle of arbitrary large radius in the upper half plane. Since $w \to 1$ as $\phi \to -\infty$, the function $\tau - i\theta \to 0$ as $\alpha^2 + \beta^2 \to \infty$ and there are no contributions from the semicircle. Therefore taking the real part yields

$$\tau(\alpha) = -\frac{1}{\pi}\int_{-\infty}^{\infty} \frac{\theta(\alpha')}{\alpha' - \alpha} d\alpha' . \tag{2.8}$$

Here $\tau(\alpha)$ and $\theta(\alpha)$ denote the values of τ and θ on the α-axis. The integral in (2.8) is a Cauchy principal value. The kinematic boundary conditions on the bottom and on the two plates imply

$$\theta(\alpha) = 0 \text{ for } \alpha < 0,\ 0 < \alpha < \alpha_c \text{ and } \alpha > 1 \ . \qquad (2.9)$$

Using (2.9) we rewrite (2.8) as

$$\tau(\alpha) = -\frac{1}{\pi}\int_{\alpha_c}^{1} \frac{\theta(\alpha')}{\alpha' - \alpha} d\alpha' . \qquad (2.10)$$

After a change of variables ($\alpha = e^{-\pi\phi}$ and $\alpha' = e^{-\pi\phi'}$), (2.10) can be rewritten in terms of the potential function as

$$\tilde{\tau}(\phi) = -\int_{0}^{\phi_c} \frac{\tilde{\theta}(\phi')e^{-\pi\phi'}}{e^{-\pi\phi'} - e^{-\pi\phi}} d\phi' , \qquad (2.11)$$

where $\tilde{\tau}(\phi) = \tau(e^{-\pi\phi})$ and $\tilde{\theta}(\phi) = \theta(e^{-\pi\phi})$.

Finally (2.4) is written in terms of τ and θ by using (2.6) and the identity

$$\frac{\partial X}{\partial \phi} + i\frac{\partial Y}{\partial \phi} = \frac{1}{u - iv} = e^{-\tau + i\theta} . \qquad (2.12)$$

This yields

$$\frac{1}{2}e^{2\tilde{\tau}(\phi)} + \frac{1}{{Fr_D}^2}\int_0^{\phi} e^{-\tilde{\tau}(\varphi)} \sin\tilde{\theta}(\varphi) d\varphi = B . \qquad (2.13)$$

With this boundary integral equation formulation, we seek two functions $\tilde{\tau}(\phi)$ and $\tilde{\theta}(\phi)$ satisfying (2.11) and (2.13) for $0 < \phi < \phi_c$. The system (2.11) and (2.13) is solved numerically in the next section, and its solution and results are presented. Once $\tilde{\tau}(\phi)$ and $\tilde{\theta}(\phi)$ are found, the free surface profile is obtained by integrating numerically (2.12).

2.3 Numerical Solution and Results

The mesh points are defined as

$$\phi_I = (I-1)\frac{\phi_c}{N-1} \qquad I = 1, 2, \ldots, N \tag{2.14}$$

and the corresponding unknowns are

$$\theta_I = \tilde{\theta}(\phi_I) \quad I = 1, 2, \ldots, N. \tag{2.15}$$

The midpoints used are defined as

$$\phi_I^m = \frac{\phi_I + \phi_{I+1}}{2} \qquad I = 1, 2, \ldots, N\text{-}1. \tag{2.16}$$

It was determined that the solutions depend on two parameters (which were chosen as Fr_D and B). There are N+1 unknowns: the θ_I and ϕ_c. The N+1 equations can be defined in the following way. Obtain N-1 equations by satisfying (2.13) at the midpoints of (2.16). To do this, first evaluate $\tilde{\tau}(\phi_I^m)$ in terms of the unknowns by evaluating the Cauchy principal value in (2.11) at the midpoints of (2.16) with a summation over the points of (2.14). The symmetry of the quadrature and of the discretization enables the evaluation of the Cauchy principal value as if it were an ordinary integral (see Vanden-Broeck (2010) for details). The last two equations force the free surface to join the plates tangentially by imposing

$$\theta_1 = \theta_N = 0. \tag{2.17}$$

The system of N+1 nonlinear equations with N+1 unknowns is solved by Newton's method. When B = 0.5, (2.4) shows that there is a trivial solution u = 1, v = 0, Y = 0 corresponding to a uniform stream with a flat free surface. In most of the calculations we chose the Bernoulli constant B = 0.500005. Calculations with other values of B close to 0.5 give qualitatively similar results. A typical profile for $Fr_D^2 = 1.08$ is shown in figure 2. If the Fr_D is increased, the vertical distance between the two plates also increases, and ultimately a stagnation point appears at the attachment point for ${Fr_D}^2 = Fr_C^2 \approx 2$. Here Fr_c is the critical Froude number for a solution to exist. Thus, there are no solutions for ${Fr_D}^2 > Fr_C^2$.

To model the experiments it was necessary to compute flows for $Fr_D^2 > 2.13$. To achieve this the model is modified by rewriting (2.13) as

$$e^{2\tilde{\tau}(\phi)} + \frac{2}{{Fr_D}^2}\int_0^{\phi} e^{-\tilde{\tau}(\varphi)} \sin\tilde{\theta}(\varphi)d\varphi + P(\phi) = B \tag{2.18}$$

where $P(\phi)$ is a prescribed distribution of pressure. Since the aim is to predict the free surface profiles near the left plate, $P(\phi)$ is chosen such that it only takes significant values near the downstream plate. Explicit calculations were for

$$P(\phi) = Ae^{[-2(\phi_N - \phi_I)]} \tag{2.19}$$

where A is a given constant.

Typical free surface profiles are shown in figure 3a. The results indicate the finite range of Froude numbers over which the cavity is expected to close on the beach, as designed. This range is only approximately 0.5 Fr_D wide (corresponding to ~0.2 Fr_L, for Froude number based on the nominal cavity length. For these experiments the Froude numbers are related by Fr_L / Fr_D

= 0.365). Therefore, concerning gas flux requirements, we can expect to have a minimum roughly corresponding to this range of Fr_L. Figure 3b presents free surface profiles for different values of the constant A appearing in (2.19). They show that the results are not sensitive to the magnitude of the pressure $P(\phi)$.

2.4 Scaling Parameters for the Cavity Flow

For the partial cavity closure, the relevant independent variables of the experiment are the free stream speed, U, the flow rate of injected air, Q, and, in the case of the small scale experiment, the surface tension, σ. Otherwise, the physical properties of the air and water were fixed. The resulting non-dimensional groups are discussed further in Section 5 and those of importance are listed in table 2. By conducting two geometrically similar, Froude scaled experiments with length-scale ratio of 14:1, we have spanned a considerable range of Reynolds and Weber numbers.

3. Large Scale Experiments

3.1 Experimental Setup

The large-scale experiments were conducted at the U.S. Navy's William B. Morgan Large Cavitation Channel (LCC), the world's largest water tunnel (Park *et al.*, 2003; Etter *et al.*, 2005). The LCC's test section is 3.05 m wide, 3.05 m tall, and 13.1 m long. For these experiments the LCC was modified by the addition of an upstream gate (Mäkiharju, 2012) to facilitate the formation of a stable free surface within the test section and diffuser. The presence of the free surface permitted continuous air injection beneath the model. It also minimized static pressure fluctuations and the accumulation of air in the tunnel during experiments. The gate was attached to the ceiling of the LCC immediately upstream of the test section inlet and projected downstream into the test section. It spanned the test section width and for the unperturbed flow, the gate's flap was held at 20^{o} with respect to horizontal, but for the perturbed flow a hydraulic actuator was used to periodically oscillate the flap with a period of 16 to 5 seconds with an amplitude of 10° to 2.5°, respectively. The flap angle was measured *via* an inclinometer (SCA121T-D03, VTI Technologies), with manufacturer specified accuracy of +/- 0.1°. The gate spanned the width of the test section, and at flap angle of 20^{o} extended down 0.97 m from the channel ceiling, displacing the flow downwards and creating a 0.44 m average flow depth above the model with a free surface in the test section. Under most flow conditions, the free surface extended into the diffuser where it returned to its conjugate depth *via* a hydraulic jump. The free surface flow over the test model was vented to the atmosphere *via* two 20.3 cm diameter valved openings, thus nominally maintaining constant atmospheric pressure above the free surface in the test section.

Figure 1 and table 1 provide a schematic and dimensions, respectively, of the large-scale test model. The freestream velocity, U, was measured via a laser Doppler velocimeter 0.22 m and 2.04 m upstream of the step, and for selected conditions velocity profiles were measured at the three downstream locations listed in table 3. Figure 4 and table 3 list all the primary measurement locations. The leading edge of the model was roughened to ensure that boundary layer transition occurred. The turbulent boundary layer 22 cm upstream of the BFS at 6.1 m/s had thickness of δ_{99} = 21 mm, and momentum shape factor $H = \delta^{*}/\theta = 1.3$. Here δ^{*} and θ are the displacement and momentum thickness, respectively. The mass flow rate of the air injected into the cavity was measured with three insertion thermal mass flow meters (640S, Sierra Instruments) mounted in the center of three steel pipes installed in parallel. The mass flow meters had an uncertainty of +/- 1% of the reading plus +/-0.5% of full scale. The mass flow rate quantity was then used, with knowledge of the cavity pressure and temperature, to determine the gas volume flux, Q.

Differences in static pressure between a reference point 2.43 m upstream of the step and atmospheric pressure, and between the reference point and cavity pressure were measured by Omega PX2300-DI10 and PX2300-DI5 wet-wet differential pressure transducers, respectively. The manufacturer specified accuracy of the pressure transducers were ±170 and ±85 Pa, respectively. The difference between the cavity pressure and free stream static pressure at the same streamwise coordinate was measured by an Omega Engineering PX760-06WCDI differential pressure transducer with manufacturer specified accuracy of ±3 Pa. The temperature of the water was maintained at 25 ^{o}C.

The establishment of a cavity was observed from skin-friction force-balance measurements and visually from continuously recorded video. The floating-plate force balances were similar to those used by Sanders *et al.* (2006), and their locations are given in table 3 and figure 4. Video was recorded continuously with four synchronized cameras (two Basler piA640-210gm and two Basler scA750-60gm cameras) controlled by Norpix Streampix 4 software. The combined view of the cameras spanned the entire cavity.

Disturbances on the interface of the cavity were measured using a point impedance probe that was traversed perpendicular to the mean flow direction. The same traverse also carried a Dwyer 173839-00 special series 166 Pitot tube and a five-electrode-rings time-of-flight probe described in detail by Mäkiharju (2012). The point impedance probes had a tip diameter of 1.1 mm, and the local impedance was detected using an AC bridge circuit with a carrier frequency of 13 kHz. The excitation voltage was supplied by HP8904A multifunction synthesizers and Stanford Research Systems lock-in amplifiers, model SRS830, were used to condition and demodulate the signals. The traverse was positioned with an accuracy of 0.2 mm. The locations of the three traverses are given in table 3 and shown in figure 4.

The signals from the three pressure transducers, three mass flow meters, gate flap's inclinometer, LCC's monitoring sensors (tunnel motor frequency and water temperature) and four force balances were simultaneously recorded *via* two PCs with National Instruments DAQs and running LabView data acquisition software.

3.2 Formation of a Stable Partial Cavity with Air Injection

As discussed in Section 2, the cavity length is dependent on the Froude number. (Recall that L/D = 7.52, relating the two relevant Froude numbers such that Fr_L / Fr_D = 0.365.) At lower than design speeds, the cavity did not reach the beach and closed on the model surface with steep impingement angles, leading to excessive air loss from the cavity; that is, the air-water interface impinged on the model before the interface wave crest and did not reach the beach for a low range of Fr_L. As the gas flux was increased for Fr_L lower than design speed, the cavity pressure increased slightly and the cavity grew in length, but the gas entrainment rate increased beyond the gas supply's capacity before the cavity reached the beach. The cavity closed on the beach for a range of $0.55 < Fr_L < 0.75$. At higher than design speeds, and high Fr_L the cavity could extend beyond the model. Also, at flow speeds above $Fr_L \sim 0.75$, with the free surface in the test section, increasing quantities of air circulated around the flow loop, and led to a perturbed and an increasingly opaque inflow. Such a perturbed inflow led to an increase in gas entrainment. The increasing and uncharacterized perturbations, and flow opaqueness limited the large-scale (LCC) experiments to conditions with $Fr_L \sim 0.8$. Also, the presence of the cavity changed the flow-loop losses in the LCC. Therefore the free stream speed slightly increased [by usually $O(3\%)$] once the cavity was established. These behaviors of the cavity were observed experimentally. However, the finite Froude number range for which the cavity closes on the beach could also be expected based on the numerical results presented in Section 2.

To find the minimum gas flux needed to establish a cavity, at the start of an experiment for each flow speed, the gas flux was increased gradually from zero until the cavity reached the beach and the flow was nominally steady. The cavity was considered established when the gas flux could be reduced without a decrease in the cavity length. This only occurred when the cavity closed on the beach. The cavity closure location could be observed to have reached the beach both visually and based on the force balances on the upstream slope of the beach. Once a stable cavity was established and the minimum establishment gas flux was determined, the gas supply was terminated. After all the air had left the cavity and the flow was at steady state, the minimum establishment gas flux was applied again to reconfirm that it would be sufficient to establish the cavity. Once the cavity was re-established and stable, so that no measurable mean quantity was changing, the search for the minimum cavity maintenance flux was initiated. The gas flux was decreased slowly in steps. Once the cavity began retreating upstream of the beach, the previously used gas flux was designated as the minimum maintenance flux. Experiments where the cavity was maintained for tens of minutes were conducted, and the cavity was found to persist indefinitely as long as the minimum maintenance flux was supplied. The results indicate that once a stable cavity is formed it remains, barring a change in gas flux or significant flow perturbations.

The non-dimensional gas flux, q, is defined as

$$q = \frac{Q}{UWH} \tag{3.1}$$

where Q is the volume flux of gas at cavity pressure and temperature, W is the cavity cross-section width (span), and H is the height of the backward facing step. The non-dimensional gas flux is expected to scale with the thickness of the closure or the related wake thickness. However, as these are not well defined, the step height H is used as a proxy. The length of the cavity, L, should not be used as the non-dimensionless gas flux is expected to be invariant for the same Fr_{L} and Re_{L} regardless of L.

Figure 5 shows the minimum non-dimensional gas fluxes, q_e and q_m. The uncertainty bars in q were defined based on the accuracy of the gas flow meter, and uncertainty in Fr_L was defined based on the uncertainty in free stream speed measurement. As the cavity reaches the beach, air entrainment from the cavity closure decreases significantly, and the gas flux can thus be reduced without loss of the cavity. The gas entrainment was likely reduced due to the angle and height of the beach, and the effect of beach height was as discussed by Arndt *et al.* (2009). The results indicate that for a single partial wave cavity (*i.e.* a cavity that reaches the beach before or at its first wave crest), the gas flux requirements are lowest within a limited Froude number range, and increase markedly with flow speed outside this range. The existence and width of this limited optimal Froude number range is consistent with the numerical results presented in Section 2, which indicate that the cavity will either terminate upstream of the beach or overshoot it for low and high Froude numbers, respectively. Also, the observed shape of the two-dimensional cavity roughly agrees with the numerical results. The minimum necessary non-dimensional gas flux of q_e = 0.027 required to establish a stable cavity occurred at Fr_L = 0.58, and the minimum non-dimensional maintenance gas flux of q_m = 0.0077 occurred at Fr_L = 0.67. In the stable range of Froude numbers, the establishment flux is roughly three times the maintenance flux.

When the cavity was stable, the gas pressure inside the cavity matched closely the static pressure of the flow at the location of the cavity detachment (*i.e*. the cavitation number based on cavity pressure approached zero), and this is consistent with the observation that the slope of the detaching cavity was horizontal (also see figure 2 and 3 that are consistent with this observation). No significant loss of gas was observed along the interface until the closure, and therefore for the stable cavity, by definition, the flow rate of air into the cavity was matched by the entrainment rate at the cavity closure.

3.3 The Cavity Interface

Figure 6 shows a photo of the typical appearance of the cavity interface at the step. As the cavity detached from the step, small surface perturbations were immediately evident. These disturbances were due to the ingestion of a fully turbulent boundary layer that separated from the step. These small-scale surface perturbations convected downstream, but they were not observed to significantly change in amplitude. These ripples were observed both visually and in the measurements from the traversing void fraction probes. Figure 7 shows a time averaged void fraction profile and compares the average interface location to that obtained from videos, and it can be seen that the agreement is satisfactory. The typical length scale of the largest visible surface ripples, λ_r, was of the order of 10 cm, making λ_r /L ~ 0.01. It is important to note that despite the presence of ripples, no significant loss of gas from the interface was observed prior to the closure region. This suggests that the air loss occurs at the cavity closure, details of which then set the required minimum gas flux to maintain a stable cavity. The perturbations present at the cavity interface may, however, affect the dynamics of the closure and hence the air loss.

3.4 The Cavity Closure and Gas Loss Mechanisms

Figure 8 shows images of the cavity closure region for the stable cavity. The stable cavity often closed on the sloped part of the surface, just upstream of the crest of the beach. Sometimes the closure could also overshoot the beach and openly vent gas from the cavity. This tendency of the closure to overshoot the beach was related to changes in the flow speed and/or due to fluctuations in the cavity gas pressure. Additionally overshoots of the beach may also be induced by auto-excitation of the cavity, as pressure pulsations from the closure feed the oscillation of the cavity surface, in turn moving the closure region. However, many conditions existed where the cavity was observed to never (or rarely) overshoot the beach, and all the air was lost *via* gas shedding from the relatively stationary closure.

The presence of a turbulent boundary layer upstream of the cavity detachment leads to pressure perturbations that impinge on the air-water interface that separates from the step. Additionally, the cavity surface has superimposed three-dimensional waves originating from the lateral sides of the cavity as discussed by Matveev (2007). The larger visually observable perturbations on the cavity surface were of the order of 10 cm. Similarly, the gas pockets shed from the closure were as large as the order of 10 cm in the spanwise direction. If we define the typical length scale as $\lambda_g \sim 10$ cm, the shed gas pockets had normalized dimensions, λ_g / L, up to the order of 0.01. The gas pockets of various sizes can be formed by any combination of three mechanisms depicted in figure 9. In the first, disturbances on the free surface of the cavity impinge on the beach and lead to the formation of gas pockets; in the second, liquid flow impinging on the beach is turned upstream as a reentrant jet that pinches off a gas pocket; and in the third, viscous forces can stretch out gas ligaments, which are subsequently separated into bubbles, similar to what occurs with plunging jets (Kiger and Duncan, 2012). The second gas entrainment mechanism was discussed by Le *et al.* (1993) and Callenaere *et al.* (2001) in the context of natural partial cavities, and similar processes were observed here and in Lay *et al.* (2010) for ventilated cavities.

The large-scale dynamics of the cavity closure also directly influenced the gas entrainment rate. Perturbations of the incoming flow will cause the cavity closure location to oscillate, as was discussed in Mäkiharju *et al.* (2010). This paper presented data from the same model when investigating PCDR under perturbed flow conditions. In several experiments, the upstream gate's flap was oscillated to produce near periodic fluctuations in the incoming flow. These fluctuations were on the order of 4% of the mean flow velocity and had a period of $T \sim 10$ seconds. This period is long compared to the time required for the flow to transit the model, such that the ratio of the advective and flow perturbation time scales, $(L/U)/T$, was of the order of 0.1. Therefore, the fluctuations were quasi-steady. The flow perturbations caused the cavity to both grow and recede to the extent that gas could be vented due to overshooting the beach, and in extreme cases the cavity could retreat sufficiently far upstream to impinge on the vertical face of the upstream beach. These perturbations led to an increased gas flux required to maintain the cavity, as the data in figure 10 show. The exact gas flux below which the perturbed cavity is lost was not determined. Instead, the points labeled as "held" and "lost" represent the smallest flux for which the cavity was still maintained and the highest flux at which the cavity was lost, respectively. These are plotted against the normalized cavity pressure fluctuations, which in turn correspond also to the percentage by which the gas is compressed. As to the scatter in the data, we should note that in the current experiments, it was not possible to vary the perturbation frequency and amplitude independent of each other. Hence, while the cavity was likely significantly more susceptible to specific frequencies, the current data only allow one to reach the simpler (and anticipated) conclusion that a larger perturbation amplitude leads to a larger excess gas flux requirement. However, for all perturbed conditions tested the cavity could still be maintained, although the required gas flux increased by as much as a factor of two.

4. Small Scale Experiments

4.1 Experimental Setup

The small-scale experiments were conducted in the Mini-LCC (MLCC) at the Marine Hydrodynamics Laboratory of the University of Michigan. This channel is a 1:14th scale model of the LCC with an additional 1.22 m extension included in both vertical legs to increase the hydrostatic pressure on the impeller. Thus, the MLCC allows for the conduct of a geometrically similar experiment with that from the large-scale experiment, including the installation of an upstream free surface forming gate. The MLCC test section is 118 cm long with a cross-section that is 21.6 cm across with 3.28 cm corner chamfers, and has 15.2 cm tall and 81.3 cm long flat windows on all four sides. Upstream of the test section is a flow conditioning section with honeycombs and screens leading to a 6:1 contraction. The flow is generated by a seven blade axial flow pump with a nine bladed stator, and it is powered by a 200 HP Toshiba 3-phase induction motor (model B2004VLF4USW) controlled by a Saftronics GP10 general purpose open loop vector AC drive (model GP10E9ST34200B1) after a speed reduction *via* a belt drive. Without a free surface, the flow speed in the MLCC can be varied from 0 to more than 25 m/s, and the test section pressure from near vacuum to 200 kPa. The tunnel also includes a degassing system enabling control of dissolved gas content. For the present experiments, the water was considered to be fully saturated at all times due to the presence of the free surface and the air entraining hydraulic jump in the diffuser which terminated the free surface.

Figure 1 and table 1 provide a schematic and dimensions, respectively, of the small-scale test model. The leading edge of the model was maintained either as smooth or roughened with randomly distributed 140 micron roughness elements in a strip starting from the model leading edge and ending 10.2 cm upstream of the backward facing step to facilitate the boundary layer transition to turbulence. The freestream velocity was measured immediately upstream of the step *via* a static Pitot tube connected to an Omega PX2300-10DI, 0 to 69 kPa transducer that had an uncertainty of ± 0.17 kPa. The free surface flow above the test model was maintained nominally at 1 atm by venting to the atmosphere. The pressure differential between the cavity and free stream was measured using an Omega Engineering PX760-06WCDI differential pressure transducer with manufacturer specified accuracy of ± 3 Pa. The pressure transducers were connected to a National Instruments DAQ NI USB-6259, and signal processing and recording was performed using Labview software. The water temperature was maintained at 23 ± 1 ^{o}C.

The injected air flux was measured using one of five Omega FL-2000 series of rotameters or one of two King Instrument Company rotameters. By using multiple flow meters, it was possible to achieve accuracy on all the airflow rate measurements of between 2% and 5% over nearly four orders of magnitude in flow rate (0.8 x10^{-6} to 1.3 x10^{-3} m^3/s). The measured volume flow rate, with knowledge of the cavity pressure and model geometry, was used to calculate the non-dimensional gas flux, q.

During the small-scale experiments, the surface tension of the flow was modified through the addition of surfactant, Triton X-100, to the water channel. The surface tension was measured using the annular slide method developed by Lapham *et al.* (1999). The resulting surface tension versus Triton X-100 concentration followed those reported by Winkel *et al.* (2004) and Liu and Duncan (2006). During these experiments, the surface tension, σ, varied between $0.034 < \sigma < 0.069$ N/m^2.

4.2 Formation of a Stable Partial Cavity With Air Injection

The cavity closed smoothly on the beach for a range of $0.5 < Fr_L < \sim 1$. Note that, unlike the large-scale experiment, stable cavities were developed at the lower Froude numbers, and these required the least amount of injected gas. While the maintenance flux reduced below the range of the flow meters, for no flow speed was a true zero-flux cavity achieved, as carefully closing off every source of gas always led to loss of the cavity given sufficient time. The minimum non-dimensional establishment gas flux, q_e, and minimum non-dimensional maintenance gas flux, q_m, were determined in a similar method as described in Section 3.2, and the results are presented in figure 11. As was the case for the large-scale cavity, the gas pressure inside the stable cavity closely matched the static pressure of flow at the edge of the cavity, and hence the cavitation number based on cavity pressure approached zero.

The sensitivity of the required gas fluxes to the boundary layer characteristics of the flow upstream of cavity detachment was tested by employing both tripped and un-tripped boundary layers prior to cavity separation. A substantial trip comprised of 140 micron roughness elements was employed to develop a turbulent boundary layer prior to the cavity separation. With this trip, the boundary layer at the BFS could be expected to have transitioned to turbulence for $Fr > 0.7$ (*i.e.* test speeds above 1.8 m/s) (figure 17.45, Schlichting 1979). In figure 11(a) the air flux required for PCDR with the boundary layer trip was compared to that required for a naturally forming boundary layer on the smooth test model, and no discernible difference can be observed in either the establishment or maintenance fluxes. Apparently, by the time the free surface reaches the closure, the influence of the initial boundary layer is much reduced. However, the effect of larger perturbations in the incoming boundary layer may have an effect, and deserve further study.

From the addition of Triton X-100, it was seen that reduction in surface tension by a factor of two had a significant effect on both the maintenance and establishment fluxes only at the lowest flow speeds, as shown in figure 11(b). However, at speeds of $U > 1.75$ m/s, the influence of the reduced surface tension was negligible. Moreover, changes in the gas entrainment varied monotonically with surface tension at the lowest speed, as shown in figure 12(a). Figure 12(b) shows the gas flux as a function of the Weber number. To facilitate the comparison, the gas fluxes have been normalized by the highest establishment or maintenance flux found at the specific Froude number, $q_{\mathrm{max},Fr}$.

These small-scale results can be compared qualitatively to those of Matveev *et al*. (2009) and Arndt *et al.* (2009). Both examined the creation of partial cavities beneath a flat surface. In the experiment of Matveev *et al*. (2009), the cavities were on the order of $0 < L < 0.2$ m, and the flow speeds were less than $U < 1$ m/s. The cavities did not close on a beach, but curved and terminated on the flat surface behind the step, as did the establishing cavities in the present experiment, and both establishing and very low-speed cavities of the large-scale experiments. In Matveev *et al*. (2009) there was very little gas lost in the cavity closure, indicating the importance of surface tension in that flow. The non-dimensional gas flux necessary to maintain the cavity was $q_m \sim 10^{-4}$ for $Fr_L \sim 0.6$, and this is on the order of the lowest flow rates of the present study at the lowest speeds.

Conversely, the experiments of Arndt *et al.* (2009) were conducted to much higher Froude numbers. Here, the cavity beach (or "cavity locker") height was only slightly less or roughly equal to the height of the separation step, and it was found that the maintenance gas flux was reduced after increasing the height of the beach. In their experiments, $0.8 < Fr_L < 4$, and $Fr_D > 1$ for all flow conditions, so cavities separated nearly parallel from the step and reached the nearly parallel beach without deflection. Figure 13 compares data from Arndt *et al.* (2009) to data measured during the current study. Comparing to data from their original model, both the maintenance and establishment gas fluxes as a function with Froude number increased with similar slopes. Data from their modified model behaves differently, and this was discussed by Arndt *et al.* (2009). We note that the two PCDR models have significantly different geometries, and the test model of Arndt *et al.* (2009) was mounted on the ceiling of the flow loop, thus ingesting the incoming TBL from the contraction. We also note that for Arndt *et al.* (2009) the minimum Froude number is close to the maximum Fr_L in the present study, and in this Fr_L range the non-dimensional gas fluxes reported in the present work are of the same order as those in Arndt *et al.* (2009).

4.3 The Cavity Interface

Images of the establishing cavity are shown for the small scale experiments in figure 14(a) and 14(b). Additionally, to contrast with figure 14(b), figure 14(c) shows the establishing cavity from the large-scale experiments. It is obvious that for the small-scale relatively less gas was lost at the same Froude number. Some of this difference can be due to surface tension's importance for this case at low Froude, Weber, and Reynolds numbers, as already seen in data of figure 11(b). Figure 15 shows the established small-scale cavity for two Reynolds and Weber numbers, and it can be seen that on the small-scale, the cavity interface was also characterized by small-scale surface perturbations, and the length scale of the largest most visible of these perturbations was $\lambda_r \sim 1$ cm, giving $\lambda_r/L \sim 0.01$. Once again, these surface perturbations did not lead to any observed gas loss along the length of the cavity. While ripples are barely visible at the lowest speeds, as the flow speed was increased, ripples at various length scales became more pronounced. Also, a decrease in surface tension by a factor of two did not qualitatively change the appearance of the surface.

4.4 The Cavity Closure and Gas Loss Mechanisms

The topology of the cavity closure varied substantially with changes in the flow speed. At the lowest speeds, the cavity would close cleanly to the beach, as seen in figure 15b, and almost no gas would be entrained in the cavity wake. Here the surface tension was sufficiently strong to prevent break-off of gas pockets at the cavity closure. Air was mostly lost by infrequent release of large gas pockets from the comparatively stationary closure with occasional shedding of a few small bubbles. At higher flow speeds, shown in figure 15a, the shedding mechanisms were qualitatively similar to that observed in the large scale experiments with the constant shedding of small bubbles and an occasional large oscillation of the cavity closure position that led to additional shedding of gas. Also, at the highest speeds the cavity would sometimes overshoot the beach and openly vent gas. And lastly, as expected, at the lowest speeds a reduction of the surface tension increased the propensity for gas loss via entrainment by the flowing liquid.

5. Scaling of the Partial Cavity Flow

For both the small and large-scale experiments, all observed air loss occurred at the cavity closure. Therefore, the critical air flux requirements are set by the physics of the cavity closure. For the partial cavity closure, the relevant independent variables are free stream speed, U, gravity, g, densities of both water and gas, ρ_w and ρ_g, viscosities of both water and gas, μ_w and μ_g, surface tension, σ, nominal length of the cavity, L, width of the model, and the angle between the closure surface and the free stream, β. The height of the backward facing step H was used as the second vertical length scale. Other important independent variables include the fluctuation velocity of the local disturbances, u', and the length scale of these disturbances, λ_r, the closure thickness, t_c, and the related wake thickness, δ_c.

The cavity pressure at the minimal air fluxes was nominally in equilibrium with the free stream pressure, and much higher than the vapor pressure, p_v ($p_c >> p_v$). Therefore the effect of the cavitation number is not considered, although it is the crucial parameter for similar natural cavities. Therefore we can write

$$Q = f\left(U, g, \rho_l, \rho_g, \mu_l, \mu_g, \sigma, H, L, W, \beta\right) \qquad (4.1)$$

There are now eleven independent parameters and three dimensions. Hence we can reduce the non-dimensionalized air flux to be dependent on eight dimensionless groups

$$q = f\left(Re, Fr, We, \frac{\rho_g}{\rho_l}, \frac{\mu_g}{\mu_l}, \frac{H}{L}, \frac{W}{L}, \beta\right) \tag{4.2}$$

The values of each of the groups are given in table 2. When comparing the present small and large-scale experiments, *Re*, *Fr* and *We* could be varied independently. Therefore, a scaling of the present data may take the following form:

$$q = f(Re, Fr, We) \tag{4.3}$$

In the following we compare the results from the different scales, and see whether they agree with the above scaling relationship. With these observations of the cavity flows over a range of Froude, Reynolds, and Weber numbers, we can make some general conclusions about the scaling of this cavity flow.

5.1 Froude Number Scaling

The shape of the cavity was strongly related to the Froude number of the incoming flow, and this was observed for both the small and large-scale experiments, as well as in the results of the semi analytical model, as discussed previously. However, the Froude number alone was not sufficient to scale the gas entrainment at the cavity closure, as this was influenced strongly by changes in the Reynolds number. Figure 16 presents the establishment and maintenance fluxes as a function of Fr_L for both experiments. The required non-dimensional gas fluxes for the large-scale experiments are typically much larger than those of the small-scale experiments. Most notably, at the lowest Froude numbers the small-scale experiments did not exhibit the drastic increase observed in the large-scale experiments. While the variation in the non-dimensional gas fluxes is markedly different, with increasing Froude number the slopes become similar. These differences are due to the effects of Reynolds and Weber number on the gas entrainment mechanisms in the cavity closure.

5.2 Reynolds Number Scaling

When the data presented in figure 16 are plotted as a function of Reynolds number, the result is figure 17. At the lowest values of *Re* (small scale), the non-dimensional gas fluxes are the lowest, and with increasing Reynolds number, the gas fluxes increase by nearly two orders of magnitude. And, the values of non-dimensional gas flux at the highest *Re* of the small-scale experiment become of the same order of magnitude as those of the large scale experiment. These observations are consistent with the change in the entrainment mechanism reported above. With an increase in Reynolds number in the small-scale experiment, the cavity closure morphed from one that shed little gas to one that began to resemble that of the large scale cavity flow. Specifically, the general appearance of the surface perturbations and shed gas clouds became qualitatively similar.

These data suggest that experiments conducted with a Reynolds number exceeding two million could be sufficient to achieve Reynolds number independence of the non-dimensional gas flux. A critical Reynolds number may exist beyond which the non-dimensional gas flux q is practically independent of *Re*. This would suggests that, if a geometrically similar experiment could be conducted at a size scale between that of the two examined here (*e.g.* $L \sim 4$ m), and at similar Froude numbers, the non-dimensional gas flux would be similar to that of the large-scale experiment.

5.3 Weber Number Scaling

The data in figures 11(b), 16 and 17 also illustrate the small influence of Weber number on the cavity closure and gas entrainment process. Here the Weber number is defined as $We = \rho_l U^2 H/\sigma$, where σ is the surface tension. At the slowest speeds and lowest *We*, surface tension is sufficient to inhibit the entrainment processes at the cavity closure, in some cases inhibiting the entrainment of almost any gas. A modest increase in *We* achieved *via* the addition of a surfactant reduced this effect, increasing the entrainment rate at the cavity closure. However, with an increase in *We* beyond ~ 600, the influence of changing the surface tension by a factor of two had negligible effect of the required gas flux.

6. Conclusions

The above results illustrate the similarities and differences of a ventilated partial cavity flow over a wide range of size scales (*i.e.* over a wide range of Reynolds numbers). At both scales, all notable air loss occurred from the cavity closure, and our observations indicate that for sufficiently high Reynolds numbers, the gas entrainment mechanisms appear to become similar, with pockets of gas continuously exiting the cavity due to a possible combination of liquid ligament formation and breakup, re-entrant flow and surface wave impingement. Surface tension, however, was only important at the lowest speeds and size scales, and its influence on the gas entrainment became negligible for Weber numbers beyond 600. The large-scale data also indicate a finite Froude number range for which the dimensionless gas flux had a minimum. This occurred when the cavity closed on the beach and the width of this Froude number range was consistent with the results of the semi analytical model. This suggests that the semi analytical model could be used to guide the initial design of the cavity and to narrow the range of geometries considered. However, a more comprehensive physical model that includes both viscous and three-dimensional effects, especially with respect the reflected wave fields on the cavity surface, should be used to refine the model geometry prior to finalizing the design.

For a single wave partial cavity, these results suggest a narrow operating speed range for optimal performance. However, based on results of Arndt *et al.* (2009), having the beach height closer to the height of the step may widen this range by increasing the highest operating speed at which the ventilation requirements remain economical. In addition, while the current results did not provide data on the possibility of establishing a multi-wave partial cavity, such an approach might lead to several discrete operating speed ranges for which the ventilation requirements have a minimum.

These results also have implications for the model testing and scaling of PCDR equipped marine craft. First, such tests should exceed a Reynolds number of at least one million based on the cavity length. This requirement should be achievable in most test basins, and would reduce the effect of surface tension on the results. This also suggests that effects from the presence of salt in the water may be negligible. Consequently, when the Reynolds number is high enough, Froude-scaled model testing should provide insight into the cavity profile and wave formation, and guide the initial estimate for the required gas fluxes. With higher Reynolds numbers, the gas entrainment rate appeared to approach Reynolds number independence. However, it is not certain whether the entrainment rates in full scale applications, with Reynolds numbers at least ten times larger than those examined here, will have similar entrainment rates.

Finally, our data suggest that modest flow disturbances can have significant implications for the required air fluxes needed to maintain the cavity, and this observation is consistent with the observations of Arndt *et al.* (2009). However, for the flow conditions covered, the gas requirements were increased at most by a factor of two, whereas in steady flow the gas flux required to establish the cavity was generally a factor of three or more higher than the gas flux to maintain the cavity. Hence, model testing of PCDR systems should be conducted with both steady and unsteady inflows. Moreover, it may be propitious to actively monitor the cavity pressure and dynamics to minimize cavity overshoot and gas loss, and such systems are, indeed, under active development, as discussed by Amromin *et al.* (2011).

Acknowledgements

The authors thankfully acknowledge the crucial support provided by the entire staff of the LCC and the machinists at the University of Michigan (Mr. Kent Pruss and Mr. William Kirkpatrick). We also acknowledge the support of Dr. Steven Zalek, Dr. Keary Lay, Mr. David Foster, Mr. Bob Etter, and Dr. Chris Chesnakas. We are also grateful to the Masters and Undergraduate students whose efforts on this project, or on related projects, contributed to the research discussed in this paper: Richard Mooney, Justin Kahl, Eloi Desrippes, Barazer Aymeric, Aymeric Leboulanger, Camille Bon, Thomas Ferretti, and Arthur de Lavernette. The research was sponsored by the Office of Naval Research under grant N00014-08-1-0215, with Dr. L. P. Purtell as program manager. We dedicate this work to the memory of Mr. Bruce Hornaday, formerly of the LCC staff.

References

Amromin, E. and Minize, I. 2003. Partial cavitation as drag reduction technique and problem of active flow control. *Marine Engineering*, **40**(3), 181-188.

Amromin, E., Karafiath, G., and Metcalf, B. 2011. Ship drag reduction by air bottom ventilated cavitation in calm water and in waves. *Journal of Ship Research*, **55**(3), 196-207.

Arndt, R.E.A, Hambleton, W.T., Kawakami, E., and Amromin E. L. 2009. Creation and Maintenance of Cavities Under Horizontal Surfaces in Steady and Gust Flows. *Journal of Fluids Engineering*, **131**, 111301 (10 pages).

Butuzov A. A. 1967. Artificial cavitation flow behind a slender wedge on the lower surface of a horizontal wall. *Fluid Dynamics*, **3**, 56–58.

Callenaere, M., Franc, J.-P., Michel, J.-M. and Riondet, M., 2001. The cavitation instability induced by the development of a re-entrant jet. *Journal of Fluid Mechanics*, **444**, 223-256.

Ceccio, S. L. 2010. Friction Drag Reduction of External Flows with Bubble and Gas Injection. *Annual Review of Fluid Mechanics,* **42**, 183-203.

Chanson, H. 1996. *Air Entrainment in Free-surface Turbulent Shear Flows,* Academic Press.

Choi, K.-S., Prasad, K.K. and Truong, T.V. (Editors) 1996. *Emerging Techniques in Drag Reduction,* Mechanical Engineering Publications Limited.

Elbing, B.R., Winkel, E.S., Lay, K.A., Ceccio, S.L., Dowling, D.R. and Perlin, M. 2008. Bubble-induced skin-friction drag reduction and the abrupt transition to air-layer drag reduction. *Journal of Fluid Mechanics*, **612**, 201-236.

Etter, R.J., Cutbirth, J.M., Ceccio, S.L., Dowling, D.R. and Perlin, M. 2005. High Reynolds number experimentation in the US Navy's William B Morgan Large Cavitation Channel. *Measurement Science and Technology*, **16**, 1701-1709.

Foeth, E.-J. 2011. Projects prove that air cavities reduce ship resistance. *Maritime Reporter and Marine News*, **12**, 16.

Gokcay, S., Insel, M., and Odabasi, A.Y. 2004. Revisiting artificial air cavity concept for high speed craft. *Ocean Engineering*, **31**, 253-267.

Gorbachev, Y. and Amromin, E. 2012. Ship Drag Reduction by Hull Ventilation From Laval to Near Future: Challenges and Successes. ATMA 2012.

Evangelista, J. (Editor), 2011. Airship of the Sea. *Surveyor, A Quarterly Magazine from ABS*, **3**, 10-15.

Kiger, K.T. and Duncan, J.H. 2012. Air-Entrainment Mechanisms in Plunging Jets and Breaking Waves. *Annual Review of Fluid Mechanics,* **44**, 563-596.

Kodama, Y., Kakugawa, A., Takahashi, T., and Kawashima, H. 2000. Experimental study on microbubbles and their applicability to ships for skin friction reduction. *International Journal of Heat Fluid Flow*, **21**, 582-88.

Kopriva, J., Arndt, R. E. A., and Amromin, E. L. 2008. Improvement of Hydrofoil Performance by Partial Ventilated Cavitation in Steady Flow and Periodic Gusts. *Journal of Fluids Engineering*, **130**(3), 031301 (7 pages).

Lapham, G. S., Dowling, D. R., and Schultz, W. W. 1999. In situ force-balance tensiometry. *Experiments in Fluids*, **27**(2), 157-166.

Lay, K. A., Yakushiji, R., Mäkiharju, S., Perlin, M. and Ceccio, S.L. 2010. Partial cavity drag reduction at high Reynolds numbers. *Journal of Ship Research*, **54**(2), 109-119.

Le, Q., Franc, J. P., and Michel, J. M. 1993. Partial Cavities: Global Behavior and Mean Pressure Distribution. *Journal of Fluids Engineering*, **115**(2), 243-248.

Liu, X., and Duncan, J. H. 2006. An experimental study of surfactant effects on spilling breakers. *Journal of Fluid Mechanics*, **567**, 433-455.

Madavan, N. K., Deutsch, S., and Merkle, C. L. 1985. Measurements of local skin friction in a microbubble modified turbulent boundary layer. *Journal of Fluid Mechanics*, **156**, 237-256.

Maki, K. J., Troesch, A. W. and Beck, R.F. 2008. Experiments on two-dimensional transom stern flow. *Journal of Ship Research*, **52**(4), 291-300.

Mäkiharju, S., Elbing, B.R., Wiggins, A., Dowling, D.R., Perlin, M. and Ceccio, S.L. 2010. *Perturbed Partial Cavity Drag Reduction at High Reynolds Numbers*. Proc. 28th Symposium on Naval Hydrodynamics, Pasadena, CA.

Mäkiharju, S., 2012. *The Dynamics of Ventilated Partial Cavities Over a Wide Range of Reynolds Numbers and Quantitative 2D X-ray Densitometry for Multiphase Flow*. Ph.D. Thesis, University of Michigan.

Matveev, K. I. 2007. Three-dimensional wave patterns in long air cavities on a horizontal plane. *Ocean Engineering*, **34**, 1882-1891.

Matveev, K. I., Burnett, T. J., and Ockfen, A. E. 2009. Study of air ventilated cavity under model hull on water surface. *Ocean Engineering*, **36**, 930–940

Park, J.T. Cutbirth J.M. and Brewer W.H. 2003 *Hydrodynamic performance of the Large Cavitation Channel (LCC).* Proc. 4th ASME–JSME Joint Fluids Engineering Conference, Honolulu, HI.

Ohtsu, I., Yasuda, Y., and Gotoh, H. 2011. Hydraulic condition for undular-jump formations. *Journal of Hydraulic Research*, **39**(2), 203-209.

Sanders, W. C., Winkel, E. S., Dowling, D. R., Perlin, M. and Ceccio, S. L. 2006. Bubble friction drag reduction in a high-Reynolds number flat-plate turbulent boundary layer. *Journal of Fluid Mechanics*, **552,** 353-380.

Schlichting, H. 1979 *Boundary-Layer Theory*, 7th English Edition, McGraw-Hill.

Vanden-Broeck, J.-M. 1980. Nonlinear stern waves, *Journal of Fluid Mechanics*. **96**, 601-610.

Vanden-Broeck, J. -M. 1996. Numerical calculations of the free- surface flow under a sluice gate. *Journal of Fluid Mechanics*,**330**, 339–347.

Vanden-Broeck, J-M. 2010. Gravity-Capillary Free-Surface Flows, Cambridge University Press.

White C. M. and Mungal, M. G. 2008. Mechanics and prediction of turbulent drag reduction with polymer additives. *Annual Review of Fluid Mech*anics, **40**, 235-256.

White, F. M. 2001. *Fluid Mechanics*, 5th Edition, McGraw-Hill.

White, C. M., Dubief, Y., and Klewicki, J. 2012. Re-examining the logarithmic dependence of the mean velocity distribution in polymer drag reduced wall-bounded flow. Physics of Fluids, **24**.

Winkel, E. S., Ceccio, S. L., Dowling, D. R., and Perlin, M. 2004. Bubble-size distributions produced by wall injection of air into flowing freshwater, saltwater and surfactant solutions. *Experiments in Fluids*, **37**, 802-810.

Winkel, E. S., Oweis, G. F., Vanapalli, S. A., Dowling, D. R., Perlin, M., Solomon, M. J., and Ceccio, S. L. 2009. High-Reynolds-number turbulent boundary layer friction drag reduction from wall-injected polymer solutions. Journal of Fluid Mechanics, **621**, 259-288.

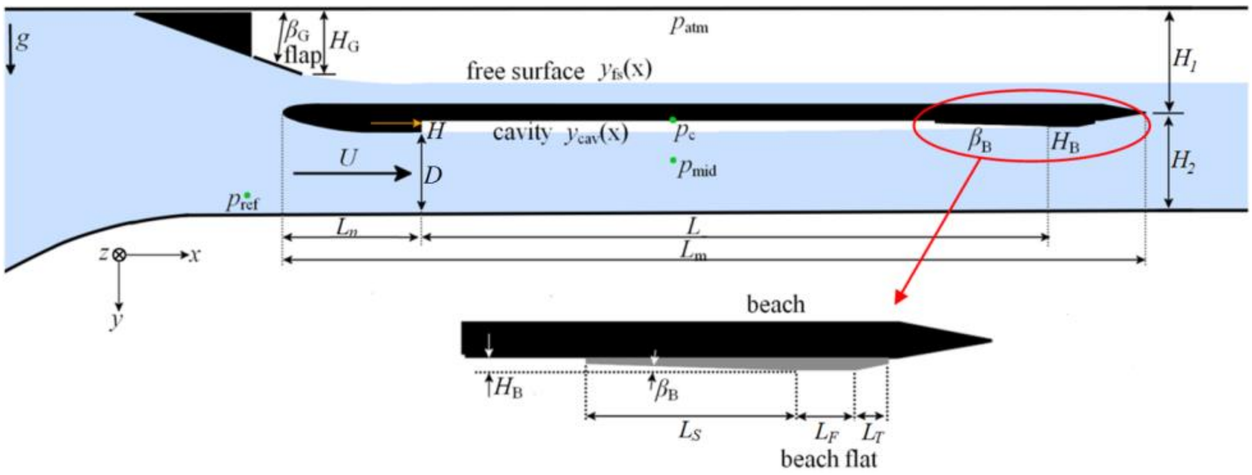

Figure 1. A schematic diagram of the gate and model in the water tunnel's test section. The dimensions of the variables listed are given in table 1. The inserted diagram details the geometry of the cavity terminating beach, shown in grey.

Parameter	Definition	Range of Values	
		Large-Scale	*Small-Scale*
Nominal cavity length	L [m]	9.25	0.654
Step height	H [m]	.178	0.0126
Length of beach flat	L_F [m]	0.56	0.0396
Length of slope	L_S [m]	1.54	0.109
Length of beach tail	L_T [m]	0.25	0.018
Model centerline to ceiling	H_1 [m]	1.58	0.112
Model centerline to floor	H_2 [m]	1.47	0.104
Height of gate from ceiling	H_G [m]	0.97	0.069
Slope of upstream section of beach	β_B [deg]	1.7	1.7
Angle of the gate's flap	β_G [deg]	20 ± 10	20
Water depth at backward facing step	D [m]	1.23	0.085
Height of beach flat	H_B [m]	0.089	0.0063
Length of model	L_m [m]	12.9	0.912
Length of nose	L_n [m]	2.01	0.147
Cavity span	W [m]	3.05	0.216

Table 1. Principal dimensions of the large and small-scale experimental setups.

Parameter	Definition	Range of Values	
		Large Scale	***Small Scale***
Free-stream Velocity	U [m/s]	5 – 7.5	1.3 – 2.5
Injected air volume flux	Q [m^3/s]	(0.3 – 2.6) x10^{-1}	(0.8 – 126) x10^{-6}
Non-dimensional gas flux	$q = \frac{Q}{UWH}$	(0.8 – 9.6) x10^2	(0.2 – 1.9) x10^3
Reynolds number	$Re = \frac{\rho_l UL}{\mu_l}$	(4.6 – 6.9) x10^7	(0.9 – 1.6) x10^6
Froude number based on cavity length	$Fr_L = \frac{U}{\sqrt{gL}}$	0.5 – 0.9	0.5 – 1.0
Froude number based on incoming flow depth	$Fr_D = \frac{U}{\sqrt{gD}}$	1.4 - 2.5	1.4 - 2.7
Weber number based on step height.	$We = \frac{\rho_l U^2 H}{\sigma}$	(0.6 – 1.4) x10^5	(0.3 – 2.2) x10^3
Density ratio	$\frac{\rho_g}{\rho_l}$	~ 0.001	
Viscosity ratio	$\frac{\mu_g}{\mu_l}$	~0.018	
Step height	$\frac{H}{L}$	~0.019	
Cavity span	$\frac{W}{L}$	~0.33	

Table 2. Experimental parameters, their definitions and range of values for both the large and small-scale experiments.

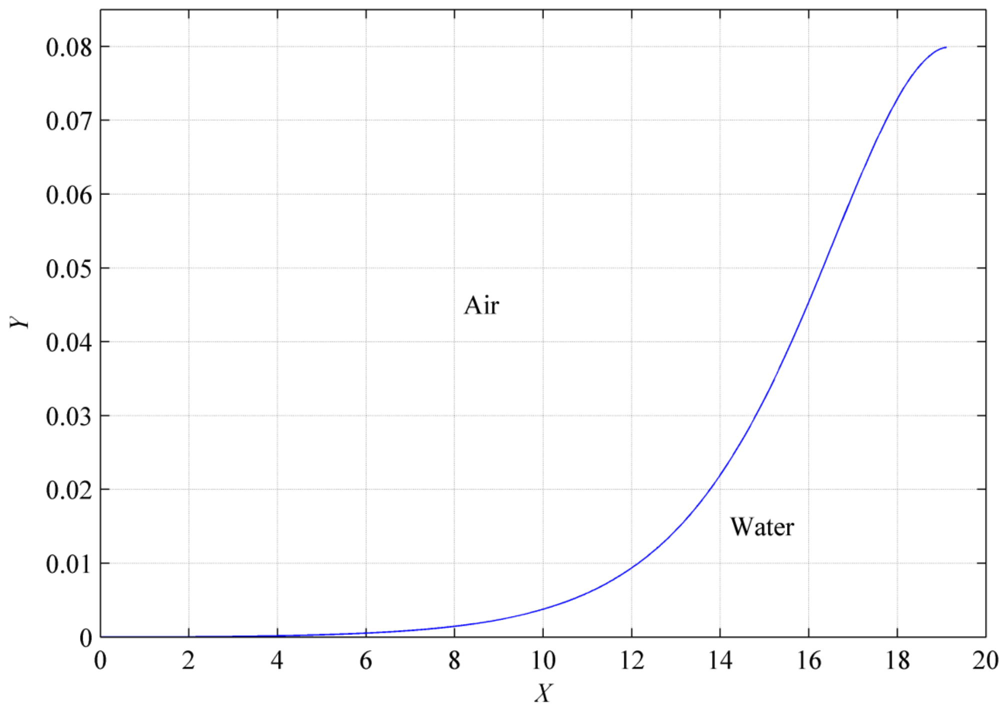

Figure 2. The computed free surface profile for $Fr_D = 1.04$. The plate to the left (not shown) is on the negative X-axis, and the flow detached from the origin. The horizontal plate (not shown) on the right extends from the last point of the free surface at $X = 19.1$.

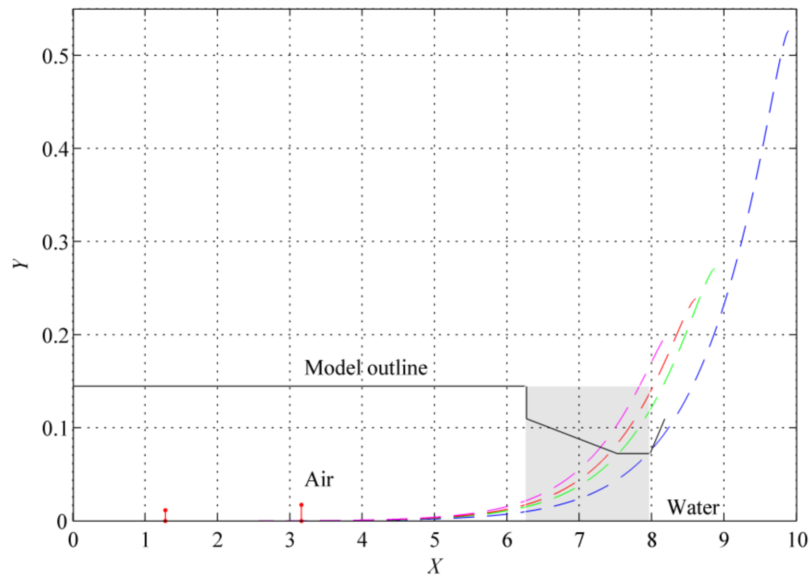

(a)

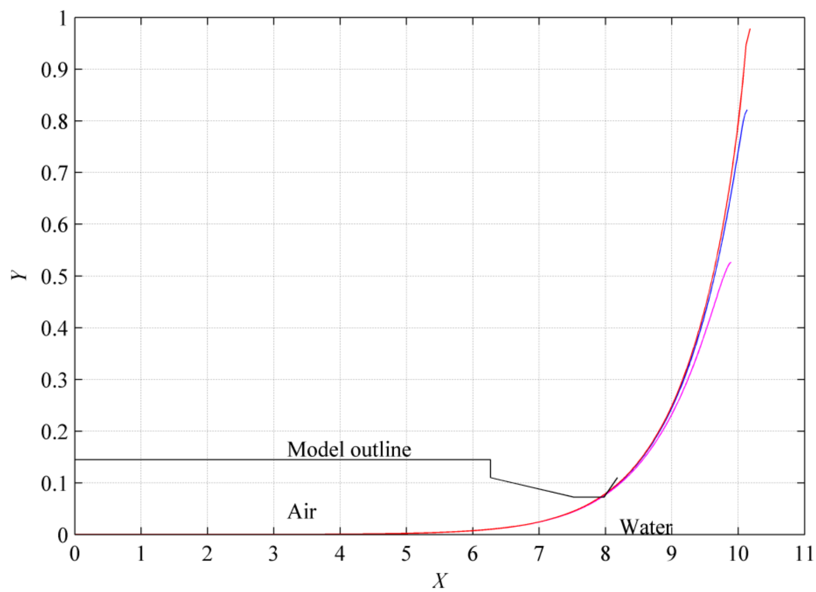

(b)

Figure 3. (a) The computed free surface profiles for various values of Fr_D (Fr_L = 0.365 Fr_D). The dashed curves from left to right correspond to Fr_D = 1.46, Fr_D = 1.66, Fr_D = 1.76 and Fr_D = 1.98, respectively. For comparison, the solid line indicates the model surface location. The red dots at X ~ 1.2 and 3.1 with a line connecting them indicate the full range of heights of the cavity surface observed at the tunnel wall. These observations based on video had uncertainty of ±0.01 Y, and the free surface on the wall exhibited oscillations, splashing, and three dimensionality. The shaded region indicates the range of the closure locations. (b) The computed free surfaces profiles for Fr_D = 1.46. The three curves from top to bottom correspond to A=0.05, A=0.1 and A=0.17 respectively.

Instrument/Object	***x* [m]**	***y* [m]**
Traverse 1	1.57	0.10...0.20
Traverse 2	3.86	0.10...0.20
Traverse 3	8.60	0.07...0.17*
Force balance #1	3.93	0.00
Force balance #2	8.58	0.07*
Force balance #3	9.04	0.08*
Force balance #4	9.56	0.09*
p_{ref} pressure tap	-2.43	1.18
p_{cav} pressure tap	4.60	0.00
p_{mid} pressure tap	4.70	0.26
LDV_{ref}	-2.04	0.27
LDV_1	-0.22	0.00...0.16
LDV_{BFS}	-0.22	0.04
LDV_2	3.93	-0.16...0.36
LDV_3	7.86	0.00...0.21
Leading edge	-2.01	-0.09
BFS/Injector	0.00	0.18/0.00

*On the beach the instruments are mounted flush with the local surface and as before $y(x)$ is the distance normal to the model surface from the instrument's mean position.

Table 3. The coordinates of the measurement and instrument locations. The base of the step is also the injector location.

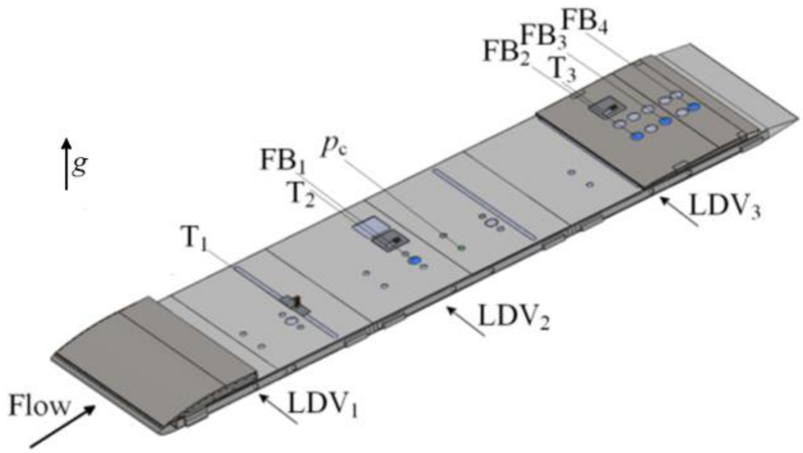

Figure 4. The large-scale model as seen from below with the primary measurement and instrument locations shown. The detailed locations are given in table 3.

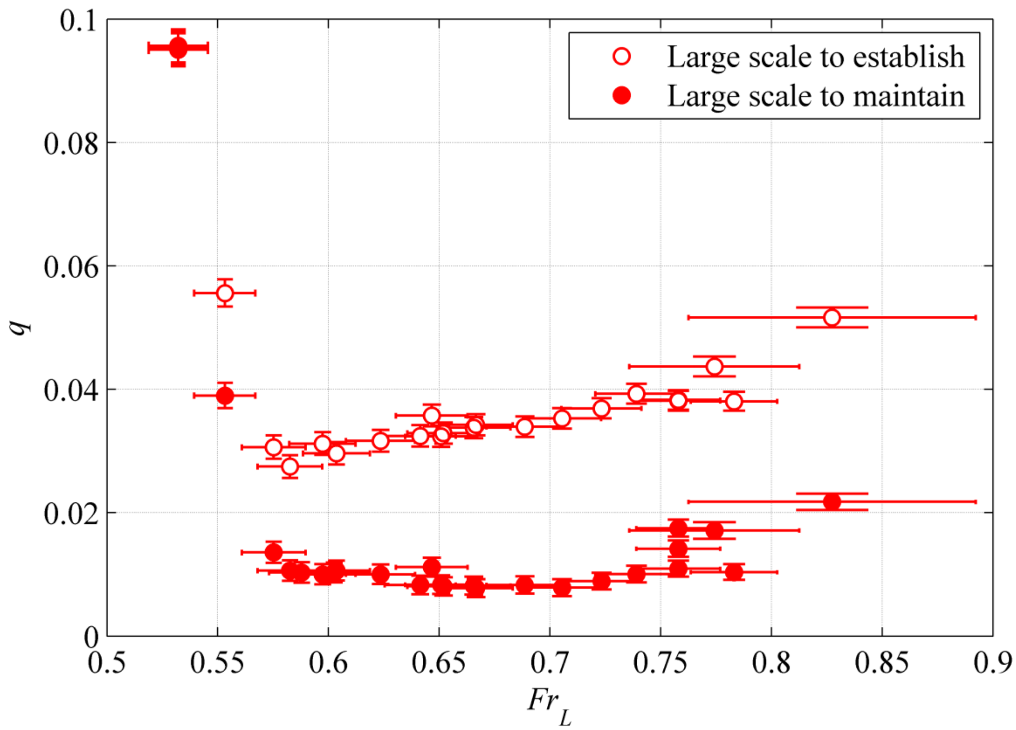

Figure 5. The non-dimensional establishment and minimum gas fluxes, q_e and q_m as a function of Fr_L for the large-scale experiment.

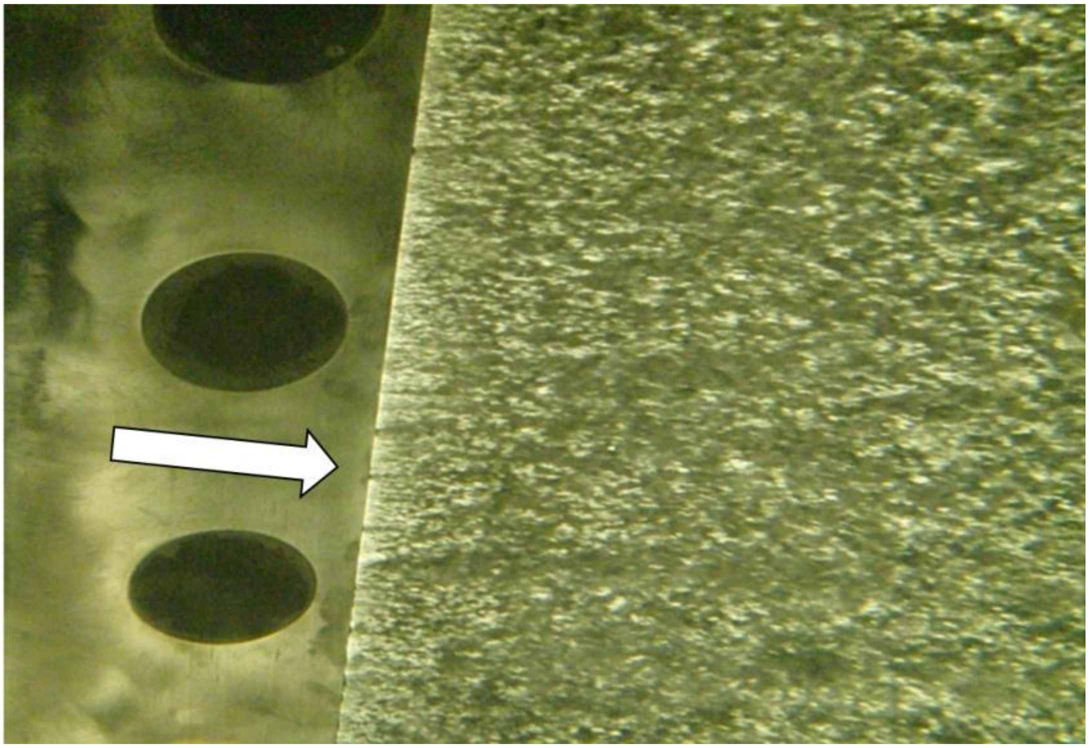

Figure 6. Photo of the cavity interface at the step for the large-scale experiment with $U \sim 6$ m/s. For scale, the black circles have a diameter of 12.7 cm. The white arrow indicates the flow direction.

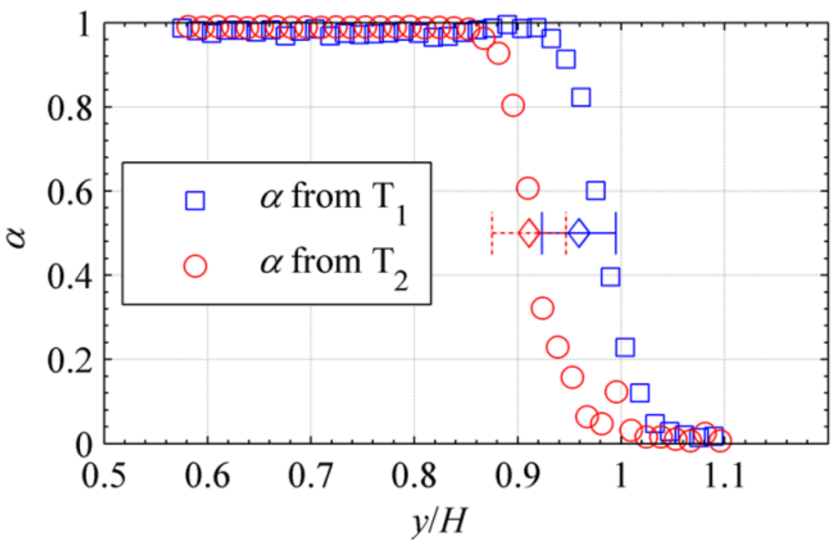

Figure 7. Time averaged void fraction, α, profiles based on data from the electrical impedance probes mounted on the two traverses, T_1 and T_2 located at x/L = 0.17 and 0.42, respectively. The void fraction profiles are compared to the local cavity thicknesses measured from the video (diamonds). The horizontal error bars show the uncertainty of the video data, ± 0.04 y/H. The free steam flow speed, U, was 5.5 m/s.

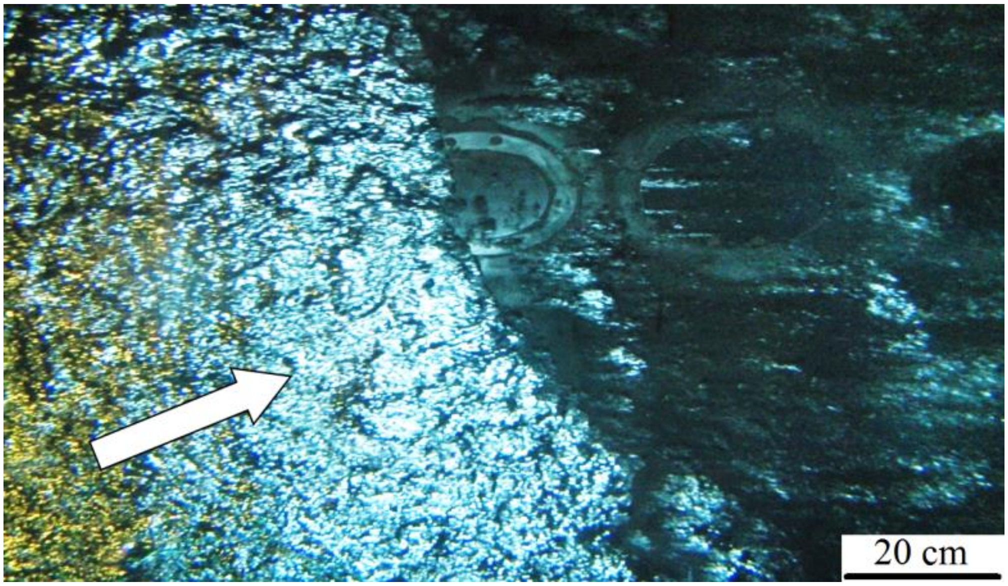

(a)

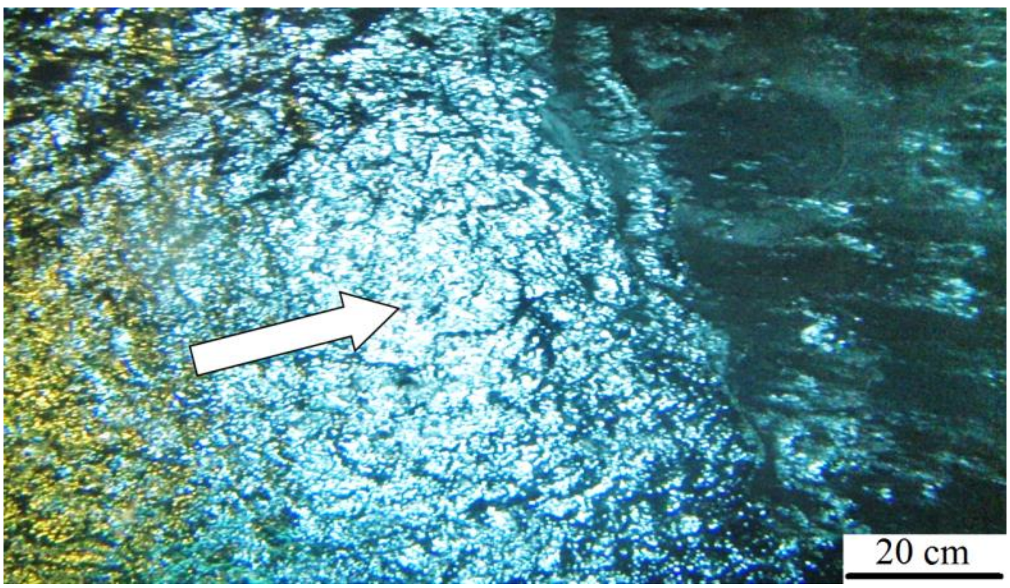

(b)

Figure 8. Images of the cavity closure region of the large-scale experiment for the stable cavity at U = 6.38 m/s. The white arrows indicate the flow direction. The small pockets of gas continuously shed from the closure can clearly be seen.

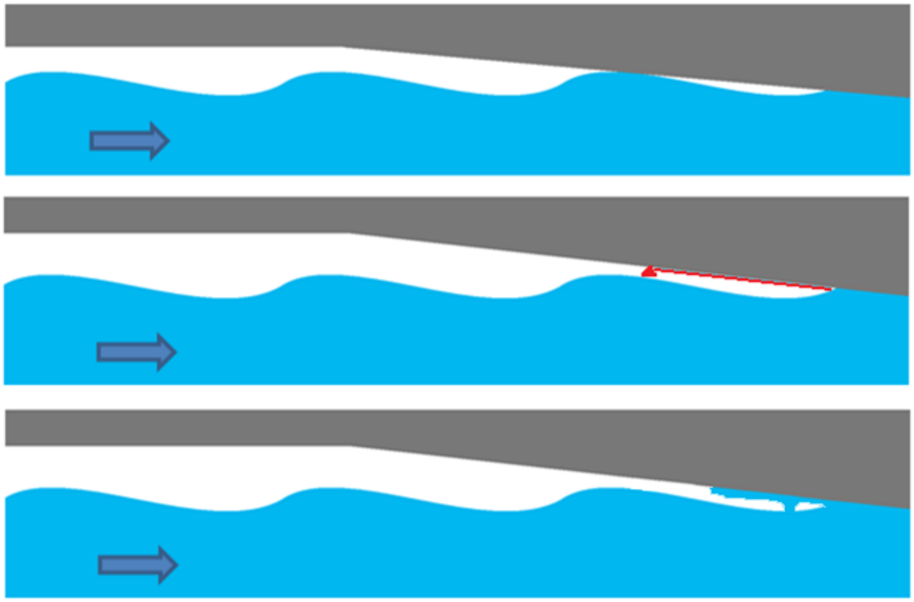

Figure 9. Three mechanisms are shown that can produce gas pockets shed from the cavity closure: (top) disturbances on the free surface of the cavity impinges on the beach and leads to the formation of gas pockets; (middle) liquid flow impinging on the beach is turned upstream as a re-entrant jet (symbolized by the red arrow pointing upstream) that pinches of a gas pocket; (bottom) ligament is stretched and part of it separates into bubbles.

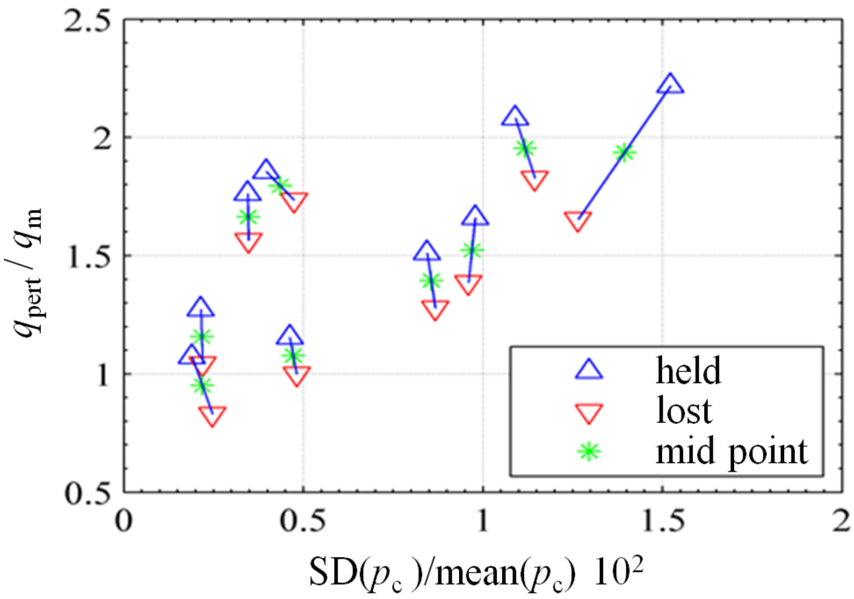

Figure 10. The variation in the required maintenance gas flux *versus* the relative perturbation amplitude defined as the ratio of the standard deviation (SD) and the mean of the pressure inside the cavity, p_c. The exact gas flux below which the perturbed cavity is lost was not measured. Instead, the upwards and downwards triangles show the last and first condition where the cavity still held or was lost, respectively.

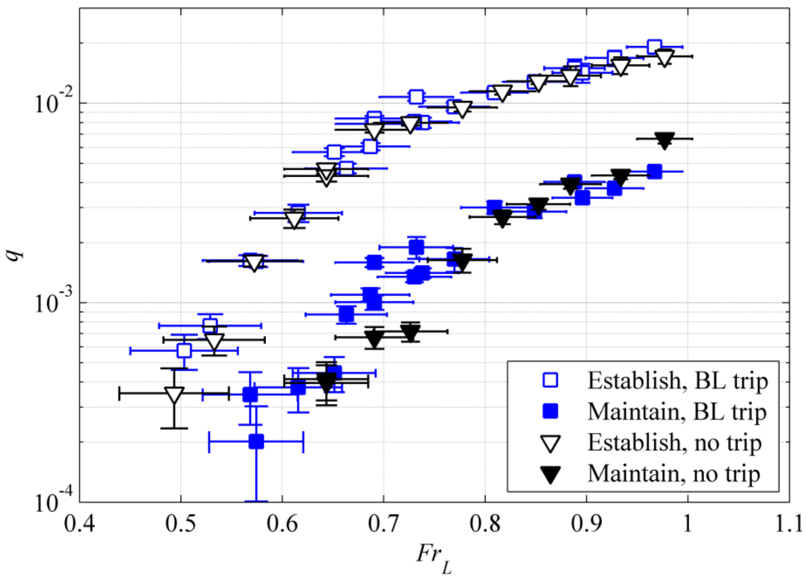

(a)

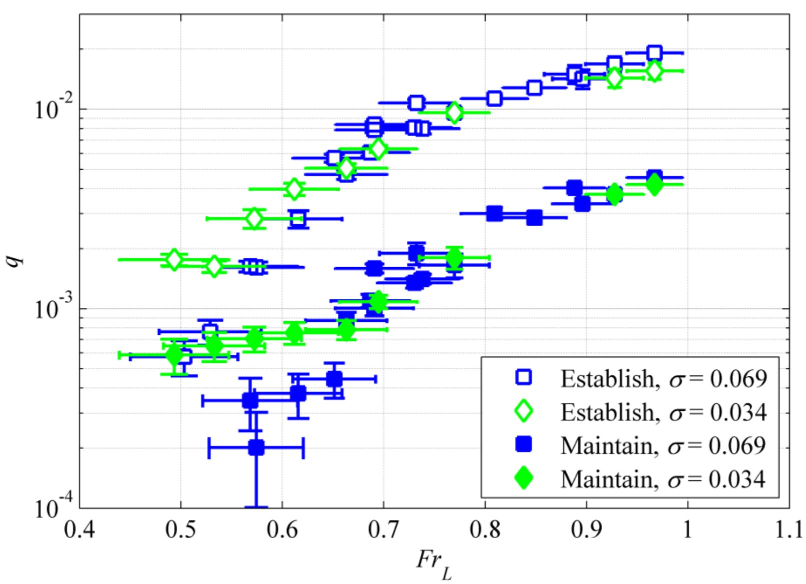

(b)

Figure 11. The non-dimensional establishment and minimum gas fluxes, q_e (open symbols) and q_m (filled symbols) as a function of Fr_L for the small-scale experiment. Data are presented for (a) the model with (squares) and without (triangles) the boundary layer trip upstream of the cavity detachment, and (b) the maximum and minimum values of surface tension, σ. For all establishment fluxes at the lower Fr, which do not have a data point for the maintenance flux, the flux was below the range of the flow meters ($< 4 \times 10^{-4}$), but larger than zero.

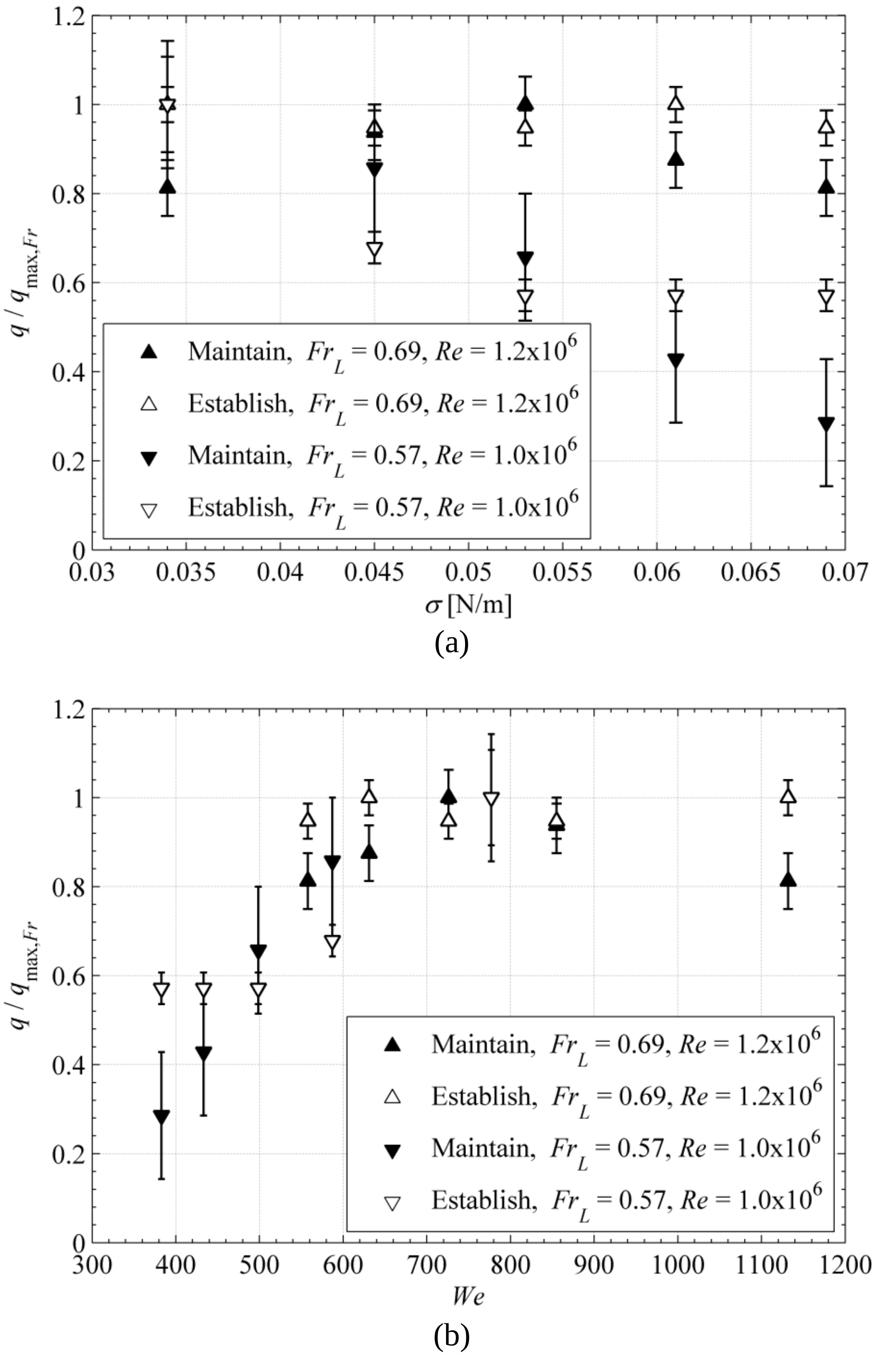

Figure 12. (a) Non-dimensional maintenance and establishment gas fluxes, q_e (open symbols) and q_m (filled symbols) as a function of surface tension, σ, for Fr_L = 0.57 and 0.69 (U = 1.45 m/s and 1.75 m/s). Surface tension measurement had an uncertainty of ± 0.002 N/m. (b) The same gas fluxes as a function of the Weber number, if the height of the step is used as the length scale. To facilitate the comparison, the gas fluxes have been normalized by the highest establishment or maintenance flux found at the specific Froude number, $q_{\max,Fr}$.

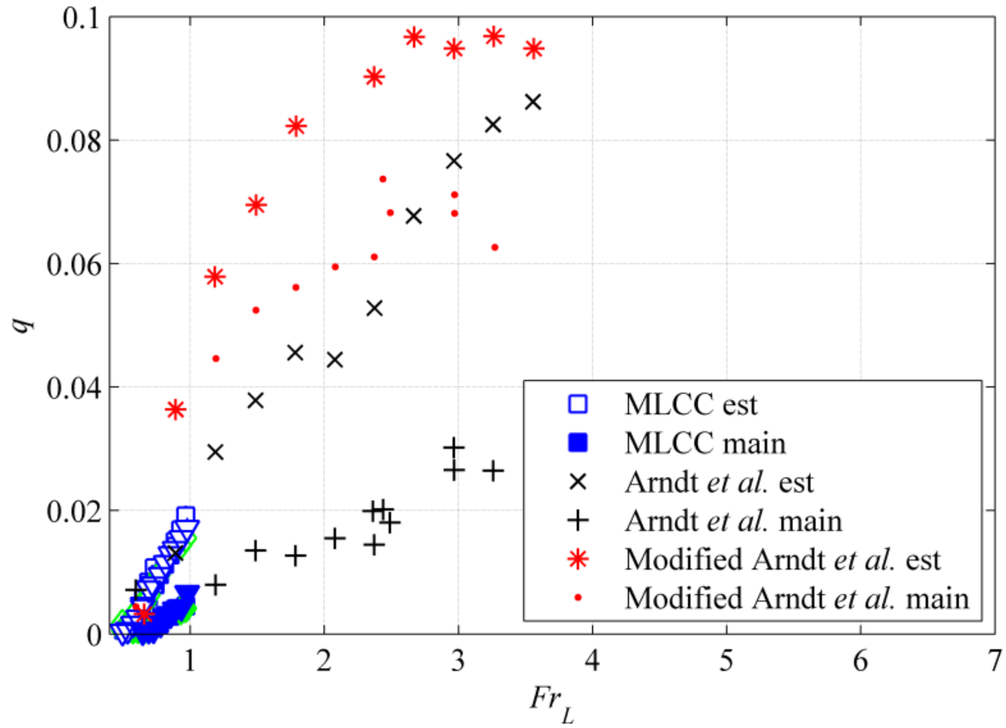

Figure 13. A comparison of the data from the small scale LCC experiments to data from Arndt *et al.* (2009). Note that the data from their original model has nearly the same slope as data from the current study.

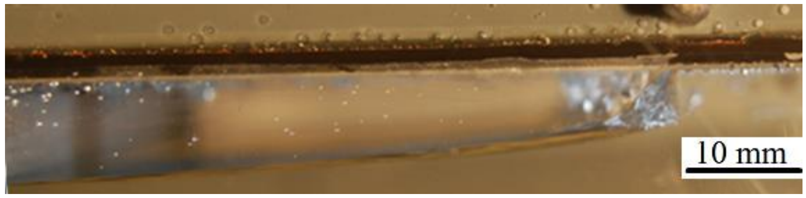

(a)

(b)

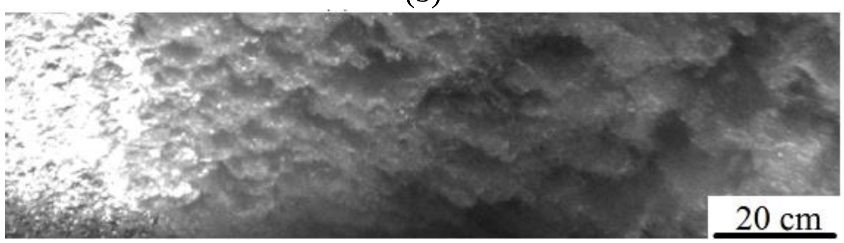

(c)

Figure 14. (a) Side view of the establishing cavity at U ~ 1.4 m/s, Fr_L ~ 0.58 in the small-scale experiment. (b) Oblique view of the same establishing cavity. (c) Close up of the establishing cavity's closure at the large-scale, where in a similar Fr_L ~ 0.6 flow the establishing cavity continuously shed large bubble clouds. Flow is from left to right.

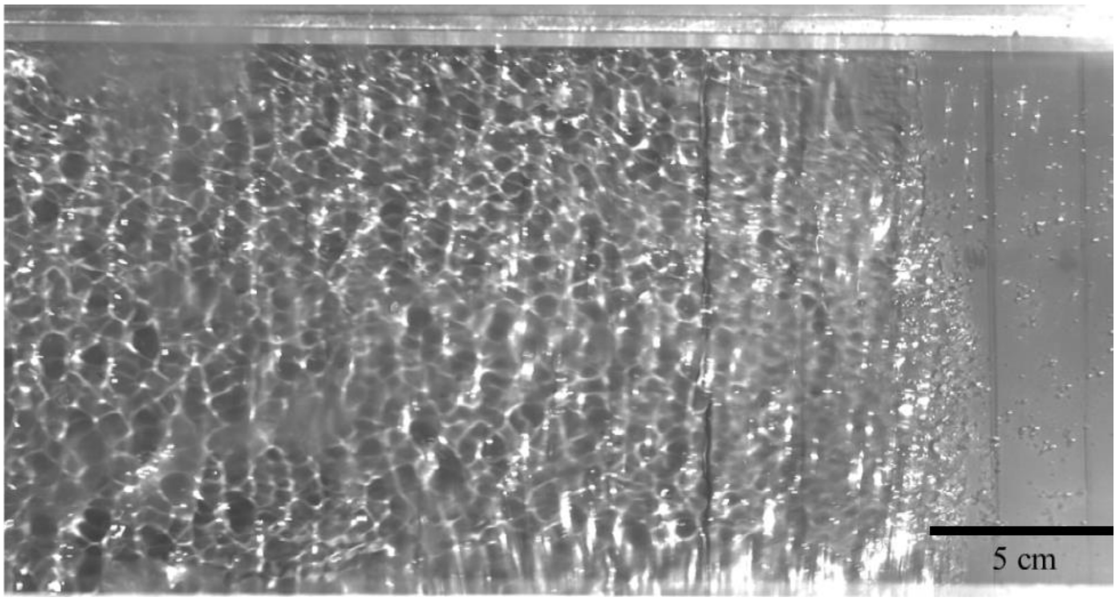

(a)

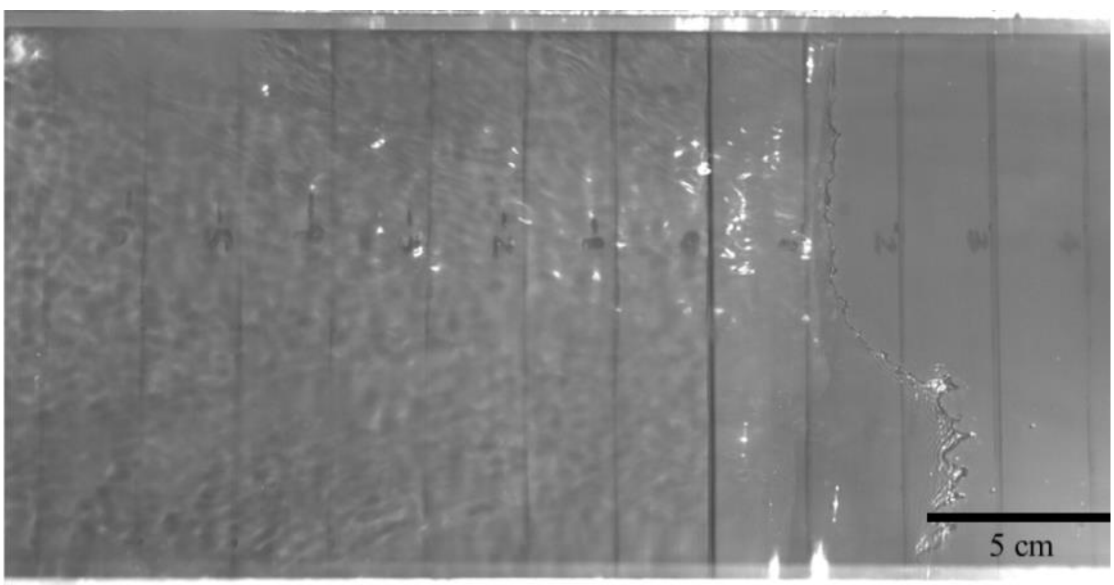

(b)

Figure 15. Images of the cavity closure for the small-scale experiments for two different Froude numbers and Weber numbers. Flow is from left to right. The backward facing step was ~65 cm to the left of the right edge of the imaged region. The cavity closure is seen ~5 cm from the right edge of the region imaged. (a) U = 2.27 m/s, Fr_L = 0.89, We = 940 and Re = 1.5 x10^6. (b) U = 1.25 m/s, Fr_L = 0.49, We = 285 and Re = 8.0 x10^5. The closure was often more two-dimensional than seen in this figure, where a portion of the cavity is just about to shed a pocket of air.

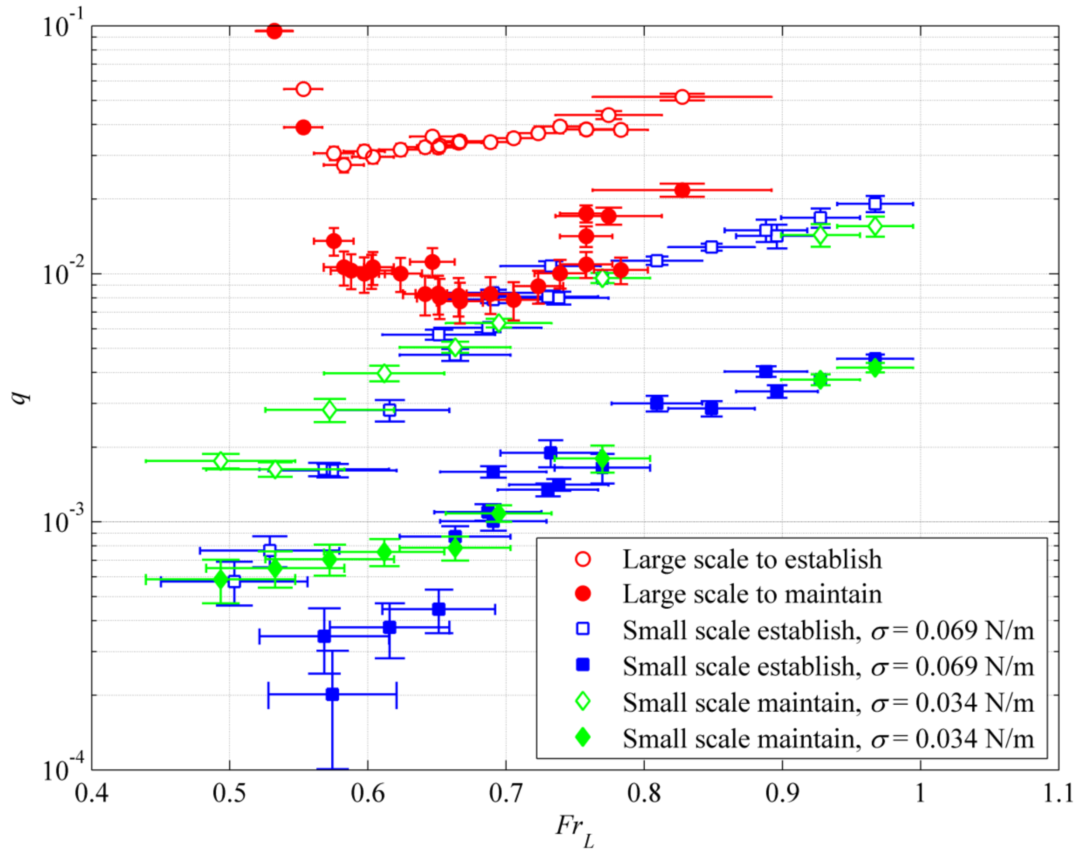

Figure 16. The establishment and maintenance non-dimensional gas flux, q_e (empty symbols) and q_m (filled symbols) as a function of Fr_L for both large- and small-scale experiments.

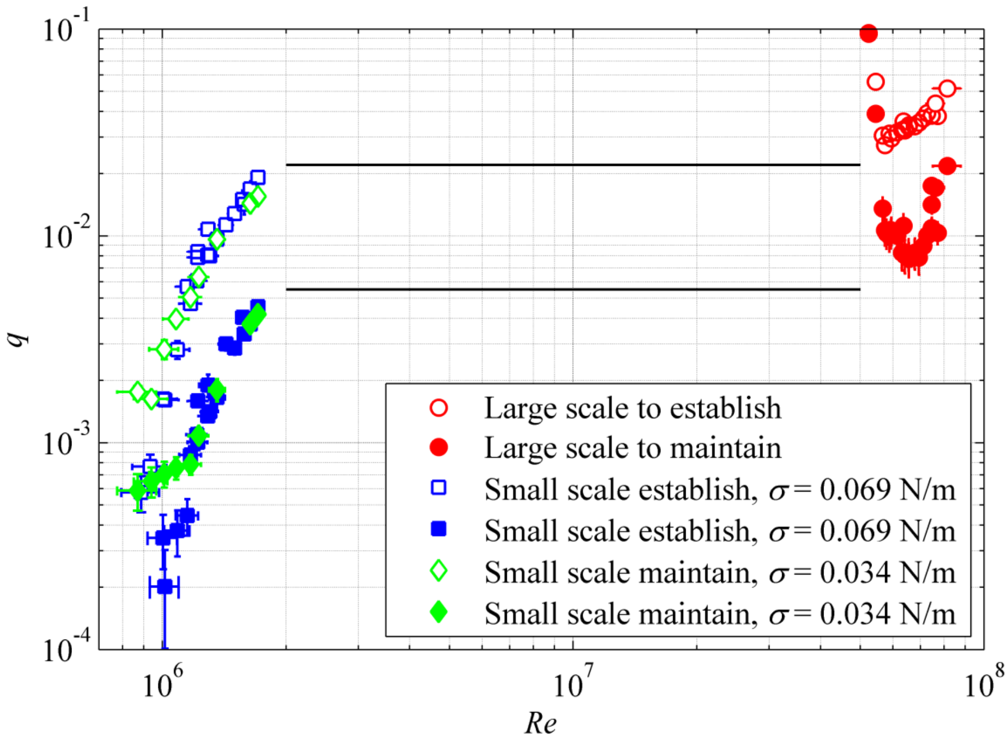

Figure 17. The data presented in figure 16 re-plotted as a function of Reynolds number.